JAEA-Research
2009-018

JAEA-Research

Fundamental Study on Flow Characteristics of Disrupted Core Pool at a Low Energy Level (Joint Research)

Koji MORITA, Ping LIU, Tatsuya MATSUMOTO, Kenji FUKUDA
Yoshiharu TOBITA, Hidemasa YAMANO and Ikken SATO

FBR System Engineering Unit
Advanced Nuclear System Research and Development Directorate

September 2009

Japan Atomic Energy Agency

日本原子力研究開発機構

本レポートは独立行政法人日本原子力研究開発機構が不定期に発行する成果報告書です。
本レポートの入手並びに著作権利用に関するお問い合わせは、下記あてにお問い合わせ下さい。
なお、本レポートの全文は日本原子力研究開発機構ホームページ（http://www.jaea.go.jp）
より発信されています。

独立行政法人日本原子力研究開発機構　研究技術情報部　研究技術情報課
〒319-1195　茨城県那珂郡東海村白方白根 2 番地 4
電話 029-282-6387, Fax 029-282-5920, E-mail:ird-support@jaea.go.jp

This report is issued irregularly by Japan Atomic Energy Agency
Inquiries about availability and/or copyright of this report should be addressed to
Intellectual Resources Section, Intellectual Resources Department,
Japan Atomic Energy Agency
2-4 Shirakata Shirane, Tokai-mura, Naka-gun, Ibaraki-ken 319-1195 Japan
Tel +81-29-282-6387, Fax +81-29-282-5920, E-mail:ird-support@jaea.go.jp

Fundamental Study on Flow Characteristics of Disrupted Core Pool at a Low Energy Level (Joint Research)

Koji MORITA*, Ping LIU*, Tatsuya MATSUMOTO*, Kenji FUKUDA*
Yoshiharu TOBITA, Hidemasa YAMANO+ and Ikken SATO

FBR System Engineering Unit
Advanced Nuclear System Research and Development Directorate
Japan Atomic Energy Agency
Oarai-machi, Higashi ibaraki-gun, Ibaraki-ken

(Received June 8, 2009)

Dynamic behaviors of solid-particle dominant multiphase flows were investigated to model the mobility of core materials in a low-energy disrupted core of a liquid metal fast reactor. Two series of experiments were performed, those were dam-break experiments and bubble visualization experiments. Verification of fluid-dynamics models used in the fast reactor safety analysis code SIMMER-III was also conducted based on the numerical simulations of these experiments. The experimental analyses show that SIMMER-III can represent effects of solid particle interaction on multiphase flow behaviors by adjusting model parameters of the particle jamming model if the particles are immersed in liquid phase. Further improvement of SIMMER-III with more generalized models is necessary to appropriately simulate interactions between solid particles in a wider range of flow conditions.

Keywords: Fast Reactor, Disrupted Core, Safety Analysis Code, Multiphase Flow, Particle Jamming

---

This work has been performed in JAEA as a joint research with Kyushu University.
* Kyushu University
+ FBR Cycle System Design Synthesis Unit

低エネルギー炉心プールの流動特性に関する基礎的研究

（共同研究）

日本原子力研究開発機構
次世代原子力システム研究開発部門　FBR システムユニット
守田 幸路*、劉 平*、松元 達也*、福田 研二*
飛田 吉春、山野 秀将+、佐藤 一憲

（2009 年 6 月 8 日受理）

液体金属高速炉の低エネルギー損傷炉心における炉心物質の流動性をモデル化するため、固体粒子が支配的な多相流の運動挙動について研究を行った。ダム堰崩壊実験および気泡可視化実験の２つのシリーズの実験を行うとともに、実験の数値シミュレーションにより高速炉安全解析コード SIMMER-III の流体力学モデルについて検証した。実験解析から SIMMER-III は、粒子ジャミングモデルのモデル・パラメータの調整によって液体中の固体粒子間の相互作用の多相流挙動への影響を模擬できることが分かった。広範な流れ条件において固体粒子間の相互作用を適切に表すためには、より一般化されたモデルを用いて SIMMER-III を改良する必要がある。

本研究は日本原子力研究開発機構と九州大学との共同研究に基づいて実施したものである。
大洗研究開発センター（駐在）：〒311-1393　茨城県東茨城郡大洗町成田町 4002
＊ 国立大学法人 九州大学 大学院工学研究院 エネルギー量子工学部門
＋ 設計統括ユニット

Contents

目次

List of Tables and Figures

1 Introduction

SIMMER-III[1),2)] is a next generation computer program used to predict the coupled neutron and fluid-dynamics behaviors of liquid metal fast reactors (LMFRs) during core disruptive accidents (CDAs). It is a two-dimensional, multi-velocity-field, multiphase, multi-component, Eulerian fluid dynamics code coupled with a fuel-pin model and a space- and energy-dependent neutron kinetics model. In order to model the complex flow phenomena in a postulated disrupted core, the mass and energy conservation equations are solved for 30 density and 17 energy components, respectively. Multi-velocity fields (up to seven for liquids and one for vapor) are modeled to simulate the movement of the different fluid components. The fluid convection is treated using a semi-implicit method.

The development of the SIMMER-III code has successfully reached a milestone with the completion of all of the physical models originally intended for simulating accident sequences of CDAs in LMFRs.[2)] It has been applied to many kinds of LMFR safety analyses, which have proved its general validity and flexibility. Meanwhile, in order to apply it more widely and reliably to the accident analysis of any future or advanced fast reactors, the improvement and assessment of SIMMER-III is still an on-going program for general types of multiphase flow problems.

In a CDA of an LMFR, there is a possibility of the formation of a disrupted core, in which solid particle-liquid multiphase flows are formed comprising a mixture of molten fuel, molten structure, refrozen fuel and solid fuel pellets, *etc*. In Fig. 1, a schematic view of this kind of disrupted core is shown. It is anticipated that such multiphase flows with rich solid phases might cause the formation of a degraded core with low mobility. Severe recriticality due to massive relocation of disrupted fuel in the core, which is a matter of great importance to the fast reactor safety, could be prevented in this situation. From a safety assessment point of view, however, it is difficult to consider the low fluidity of a mixture of solid particles and liquid components in the present CDA analysis on a conservative basis. This is because we have insufficient knowledge about the behavior of multiphase flows with rich solid phases in a postulated disrupted core, regardless of its importance to the recriticality event.

In the SIMMER-III code, there are some models that take consideration of the extra influence of solid particles on the behavior of multiphase flows, such as the particle viscosity model and the particle jamming model.[3)] The particle viscosity model, which is based on equations proposed by Russel,[4)] was introduced to model the effective increase in the fluid viscosity of materials due to the existence of solid particles in the molten mixture, while the particle jamming model was used to ensure that the volume fraction of solid particles does not exceed a maximum packing fraction in computational cells. These models were initially introduced to SIMMER-III to consider the effect of solid phases in channel flows. Besides, the viscous diffusion term, i.e. the momentum diffusion term,[5)] was implemented for the purpose of investigating the effect of bubbles on the behavior of a molten pool. The particle viscosity model is applied to the fluid viscosity in both the viscous diffusion term as well as the fluid-fluid drag term. Despite the existence of these models, however, little work has been performed with regards to verifying the validity of the SIMMER-III code on simulating the dynamic behaviors of pool multiphase flows with rich solid particles.

On the other hand, concerning multiphase or two-phase flows with rich solid particles, significant advances were made in numerical modeling during the past few decades, especially in gas-solid flows. For example, Gidaspow and his co-workers worked on a two/multi-fluid approach,[6),7)] while Tsuji and his co-workers[8),9)] concentrated their efforts on establishing a distinct element model. Gera et al.[9)] has made a comparison of the two approaches. Generally, the Eulerian-Lagrangian approach is well applied to simulations with a small number of particles, while the Eulerian two/multi-fluid model is a preferred method for simulating the fluid dynamics of highly loaded particle flows.[10),11)] However, while all of the above works are mainly concerned with fluidized beds, the available experiments were performed with small solid particles or fine powders mainly in a two-dimensional column, which may be very different from the pool multiphase phenomena in a postulated disrupted reactor core with relatively larger solid particles mixed with melted fuel *etc*.

In the previous study,[12)] a series of liquid dominant multiphase flow experiments was performed to verify SIMMER-III in simulating the pool flows with rich solid particles. Sensitivity analysis of models showed that the viscous diffusion term coupled with the particle viscosity model does not contribute to improve the simulations and further experiments for the verification of the particle jamming model are necessary. Although the viscous diffusion term has been introduced to SIMMER-III for the investigation of the effect of bubbles on the behavior of a molten pool, SIMMER-III without this term reasonably represented the behaviors of the performed experiments. The simulation results indicated that although there is no consideration of an additional pressure field for the solid phase in the momentum equation of the solid phase, SIMMER-III can still be applied for representing the behavior of multiphase flows with solid phase when the liquid phase is dominant in the dynamic behavior. In this study, therefore we performed two series of solid-particle dominant multiphase flow experiments, including dam-break experiments and bubble visualization experiments. Verification of SIMMER-III was also conducted based on numerical analyses of these experiments.

This report is organized as follows. Simulation models and methods of SIMMER-III are described in Chapter 2. The dam-break experiments and SIMMER-III analyses are explained in Chapter 3. Chapter 4 presents the bubble visualization experiments and SIMMER-III analyses. In the last chapter, concluding remarks are drawn.

2 SIMMER-III models and methods

2.1 Multiphase flow models

In the SIMMER-III code, conservation equations are written for independent variables in a unit volume. Therefore, the mass equation is expressed with respective to macroscopic density, for which formula $\bar{\rho} = \alpha / \upsilon$ is used, where α is the volume fraction and υ is the specific volume.

The experimental conditions described in Chapters 3 and 4 indicate that there is no necessity to consider heat and mass transfers, so the experimental three-phase flows of solid particles, water and nitrogen gas, which are, respectively, assigned to different velocity fields, can be modeled by the following three-fluid mass and momentum equations:[1),5)]

$$\frac{\partial \bar{\rho}_q}{\partial t} + \nabla \cdot (\bar{\rho}_q v_q) = 0 \tag{2-1}$$

$$\frac{\partial \bar{\rho}_q v_q}{\partial t} + \nabla \cdot (\bar{\rho}_q v_q v_q)$$

$$= -\alpha_q \nabla p + \bar{\rho}_q g - K_{qs} v_q + \sum_{q'} K_{qq'} (v_{q'} - v_q) + VM_q - \left[\nabla \cdot (2\alpha_q \mu_q S_q) - \nabla (\frac{2}{3} \alpha_q \mu_q (\nabla \cdot v_q)) \right] \tag{2-2}$$

where q and q' (= 1, 2, and 3) represent the components of the three phases, v is the velocity vector, VM_q is the virtual mass term, S_q is the strain rate, and K_{qs} and $K_{qq'}$ are called momentum exchange functions, which will be explained later.

The above conservation equations indicate that in the SIMMER-III code with a consideration of 30 density components in 8 velocity fields, all phases are assumed to share the same pressure field, i.e. there is no consideration of the solid-phase pressure and the solid-phase stress tensor, which have been considered by some researchers in the modeling of gas-solid fluidized beds.[6),7),10),11),13)]

The overall fluid dynamics solution algorithm of the SIMMER-III code is based on a time-factorization approach called the four-step method developed for AFDM, in which intra-cell interfacial area source terms, momentum exchange functions *etc*. are determined separately from inter-cell fluid convection.[14)]

2.2 Momentum exchange functions and viscous diffusion term

In the momentum Eq. (2-2), the term $K_{qs} v_q$ is the fluid-structure drag while K_{qs} is called the momentum exchange function between velocity component q and structure. In pool flow, the influence of structure could be ignored, the detail description of K_{qs} will not be described here, but it is necessary to be pointed out that in the SIMMER-III code, K_{qs} has more functions than the above definition. Pressure drop coefficients are added to K_{qs} in order to consider the pressure drop through an orifice, and the effect of the particle jamming model, which will be explained later, can also be taken into consideration though K_{qs}.

Because both theoretical and experimental knowledge of details is limited for a multi-component multi-velocity flow, the fluid-fluid drag term $\sum_{q'} K_{qq'}(v_{q'} - v_q)$ of Eq. (2-2) is formed based on an analogy from engineering correlations of the steady-state two-velocity flow. $K_{qq'}$ is called the momentum exchange function between components q and q', among which the $K_{qq'}$ between continuous and discontinuous components are modeled based on Ishii's drag-similarity hypothesis.[15] The mathematical form for $K_{qq'}$ is defined as

$$K_{qq'} = A_{qq'} + B_{qq'} \left| v_q - v_{q'} \right| \tag{2-3}$$

where $A_{qq'}$ is called the viscous term while $B_{qq'}$ stands for the turbulent term. The quantities $A_{qq'}$ and $B_{qq'}$ are functions of flow regime, volume fraction, velocities, binary contact areas, and viscosities. Detailed definition of $K_{qq'}$ can be referred to the work of Tobita et al. in 1991.[16] In the SIMMER-III code, this fluid-fluid drag term is simulated for the purpose of considering the intra-cell momentum transfer between different velocity components.

The eighth term in the left hand side of Eq. (2-2) is the so-called viscous diffusion term. In the SIMMER-III code, this term is simulated to represent the inter-cell momentum transfer of velocity component q. The viscous diffusion term was initially introduced to the SIMMER-III code for the investigation of the effect of bubbles on the behavior of a molten pool.[5] In the previous study,[12] however it was found that the viscous diffusion term coupled with the particle viscosity model does not contribute to improving the simulations. Here, taking off the viscous diffusion term, the momentum Eq. (2-2) for modeling the three phase multiphase flow experiments becomes

$$\frac{\partial \bar{\rho}_q v_q}{\partial t} + \sum_{m \in q} \nabla \cdot (\bar{\rho}_m v_q v_q) + \alpha_q \nabla p - \bar{\rho}_q g + K_{qs} v_q - \sum_{q'} K_{qq'}(v_{q'} - v_q) - VM_q = 0 \tag{2-4}$$

2.3 Particle viscosity model

In order to simulate the penetration of molten materials into, and their blockage formation in, a cold structure channel during CDAs, it is important to simulate the effective increase of the fluid viscosity of the materials due to the existence of solid particles in the molten mixture. Russel[4] has made a comprehensive report relevant to the viscosity increase due to the solid particles and has proposed the following formulation for colloidal suspensions:

$$\frac{\mu_C}{\mu_L} = \begin{cases} 1 + 2.5\alpha_P + 6.2{\alpha_P}^2 + O({\alpha_P}^3) & \alpha_P \le 0.3 \\ \dfrac{8}{9} \dfrac{(\alpha_P/\alpha_{MP})^{1/3}}{1-(\alpha_P/\alpha_{MP})^{1/3}} & 0.3 \le \alpha_P \le \alpha_{MP} \end{cases} \tag{2-5}$$

where μ_C is the effective viscosity of the continuous liquid phase, μ_L is the viscosity of the continuous liquid phase, α is the volume fraction, the subscripts L and P stand for liquid and solid particles, respectively, and α_{MP} = 0.62 is the maximum volume fraction of solid particles.

The above formulation was verified by experimental data[17),18)] using water and polystyrene

latex-particles with a diameter of 0.1 to 1.12×10^{-6} m. Although we need discussion on the applicability of Eq. (2-5) to systems with much larger particles, this issue is outside the analysis range of this study.

A particle viscosity model based on Eq. (2-5) was introduced to the SIMMMER-III code by replacing it with the following formulation:[3)]

$$\mu_C = \mu_L \left\{ \frac{\alpha_L}{\alpha_L + \alpha_P} + \frac{f\alpha_{MP}\alpha_P}{\alpha_{MP}(\alpha_L + \alpha_P) - \alpha_P} \right\} \tag{2-6}$$

where f is a model parameter. Tailored from Eq. (2-5) proposed by Russel, Eq. (2-6) is used in the SIMMER-III code with f = 5.0. This reformatted equation realizes the smooth change of effective viscosity over the wide range of particle volume fraction. Fig. 2 shows the comparison of effective viscosity between Eqs. (2-5) and (2-6) as a function of effective volume fraction $\alpha_P/(\alpha_L + \alpha_P)$ of solid particles in the liquid and solid-particle phases.[3)] In SIMMER-III calculations, a numerically large constant value is assigned to μ_C/μ_L when $\alpha_P/(\alpha_L + \alpha_P)$ exceeds α_{MP}.

With the application of Eq. (2-6) in SIMMER-III, μ_C is used to substitute the conventional liquid viscosity appearing in the calculation of the quantities $A_{qq'}$ and $B_{qq'}$ as well as μ_q in the viscous diffusion term. Although the particle viscosity model was originally introduced to SIMMER-III in the simulation with respect to the penetration and blockage formation of molten materials to a structure channel, little work has been done toward the verification of its effect on the simulation of pool multiphase flows with rich particles. The influence of this particle viscosity model on the dynamic behavior of the particle bed in a liquid pool has been discussed in the previous study.[12)]

2.4 Particle jamming model

A particle jamming model was also developed in SIMMER-III in order to appropriately simulate the blockage formation of molten materials when penetrating into a structure channel. Considering a situation in which solid particles flow into a cavity and accumulate from the bottom, solid particles usually cannot occupy all of the space in the cavity, and thus their volume fraction has a certain maximum value. This phenomenon is called “particle jamming.” As shown by Fig. 3, in SIMMER-III, this is modeled by inhibiting the inflow of solid particles into a computational mesh cell when the volume fraction of solid particle in the cell exceeds a maximum packing fraction by assigning a large value to the momentum exchange function at the cell interface.

The idea behind the particle jamming model is to define a function of the volume fraction of particles, which increase exponentially with the increase of particle volume fraction and become large as the maximum packing fraction is approached in a computational mesh cell. Using the same function adopted by SIMMER-II,[19)] a particle jamming function was introduced to the SIMMER-III code. The function is based on the assumption that when the solid particle volume fraction is smaller than a defined maximum packing fraction, the function remains equal to zero, but when the solid particle volume fraction approaches the maximum packing fraction, then the function will rapidly increase to an infinite value. This particle jamming model is expressed by the following formulation:[3)]

$$\phi = \max\left\{1 - \frac{\max(\alpha_P - \alpha_{PJ\max}\beta_{PJ}, 0)}{\alpha_{PJ\max}(1-\beta_{PJ})}, 0.1\right\}^{C_{PJ}} - 1 \qquad (2\text{-}6)$$

where $\alpha_{PJ\max}$ = 0.7 is the maximum volume fraction of solid particles while β_{PJ} = 0.95 is the fraction of $\alpha_{PJ\max}$ above which the particle jamming model is applied. The model parameter C_{PJ} is set to –10.0. This function remains zero (*i.e.* ϕ = 0.0) if α_P is not larger than $\alpha_{PJ\max}\ \beta_{PJ}$ and increases rapidly to $0.1^{C_{PJ}} - 1$ (i.e. $\phi = 0.1^{C_{PJ}} - 1$) when α_P exceeds $\alpha_{PJ\max}\ \beta_{PJ}$.

In the SIMMER-III code, ϕ is added (not multiplied) directly to the momentum exchange function K_{qs} between liquid phases and structures of the momentum Eq. (2-2). For pool flows where the effect of the structure is negligible, through this addition mathematic treatment, the effect of particle jamming can be considered by applying $K_{qs} = \phi$ to Eq. (2-2).

The particle jamming model was also mainly introduced for structure channel flows, and thus knowledge about its influence on pool multiphase flows with rich solid particles is limited. In this study, the effect of this model will be discussed.

3 Dam-break experiments

3.1 Experimental apparatus and method

Dam-break experiments are performed using a rectangular water tank made from transparent acrylic resin under the atmospheric environment. Both the length and height of the water tank are 260 mm while its wide is 100 mm. Fig. 4 shows a schematic view of the dam-break experimental apparatus. A dam board is fixed at a location of 64 mm away from the left wall of the water tank in order to hold the mixture of water and solid particles being in a stagnation state in the beginning of each experiment. Different experimental cases are performed by changing the particle bed height h or the water height H as shown in Fig. 4. When experiments begin, the dam board will be pulled out from the water tank with a vertical velocity of about 3 m/s by an external force system. At the same time, the water-particle dam breaks and dam-break flow forms. A high-speed camera, which has a frame rate of 200 fps, is used for recording the movement observed in the rectangular water tank.

3.2 Experimental conditions

Solid particles used in all dam-break experimental cases are the plastic particles (YB balls), which have a density of 1010 kg/m^3 closing to the density of room temperature water, with smooth surface. This kind of particle is used because with a similar density to water, it would serve much better for the purpose of investigating the influence of solid-solid interactions on the multiphase flow behaviors.

A lot of experimental cases with different combinations of the water height H and the particle bed height h were performed. In this report, experiments with a fixed H (H = 128 mm) and variable h will be mainly analyzed. For cases with H < h, an extreme case, where H = 0 mm, will be shown as a sample explanation. Experimental conditions of five selected typical cases are shown in Table 1. The name of all cases, in which W stands for water while P represents particles, reflects the ratio of the water height and particle bed height. The case W8_P0 will be analyzed as a reference case since in this case no particles exist. From cases W8_P5, W8_P7, to W8_P8, the water height is fixed as 128 mm while the particle bed is increased from 80 mm to 128 mm. In the case W0_P8, there is no water existing but an air solid-particle two phases flow formed.

3.3 Experimental results

Before presenting the experimental results, visible errors existing in the experimental images as well as definition of an experimental parameter goes first here. Fig. 5 shows two sample images of the case W8_P8. For a direct observation and comparison, the back wall of the water tank was marked by 5 × 5 uniform grids. The two images in Fig. 5 show an area including 5 × 4 grids.

In the vertical Z direction, as measured in the beginning of the case W8_P8, both the water and the particle bed height are 128 mm, however, the recorded images show a height very close to 3 grids, which is 156 mm. This indicates that when performing this experiment case, error exists in the visual angle between the camera and the water tank. Actually, in all other cases, the same error also exists. Therefore, to compare the exact height (for example, the height along the right wall or left wall that the movement can arrive.) in

the images is of great difficult, while comparison between the general movement trends is meaningful and possible.

In the horizontal X direction, 3D images were recorded with the visible left and right walls of the water tank, which cause the length of the water tank looks more than 5 grids. XD, which is the distance between the left wall and the front head of the flow as shown in Fig. 5, will be analyzed as an experimental result. Therefore, in order to consider this experimental error, the experimental results of XD are calculated in a relative way by keeping the total visible length of the recorded images being 260 mm as shown in the figure.

Fig. 6 presents the time for the dam-break flow front head to arrive at the right wall of the water tank of all experimental cases listed in Table 1. A rough conclusion is that the more solid particles exist, the longer it takes for the front head of the flow to arrive at the right wall. Curves showing variations of XD with time of three selected experimental cases are also given in Fig. 6. The slopes of these curves indicate that the speed in the dam-break flow is very different from each other among cases W8_P0, W8_P5 and W8_P8. The reference case W8_P0, in which there is no solid particles, has the fastest speed. Considering the close densities between water and solid particles, different from the experiments analyzed in the former chapters, results of the dam-break experiments indicate that the solid phase has a prominent influence on the multiphase flow phenomena.

Figs. 7 to 11 show the dam-break flow images of the five experimental cases, respectively. All images in those figures represent the same area of 260 mm × 208 mm as the 5 × 4 grids images in Fig. 5. During a two seconds period, the flow front head climbs along the right wall of the tank three times in the reference case W8_P0 while only twice in both cases W8_P5 and W8_P7. This indicates that the existence of solid particles caused larger and faster loss of the total momentum probably because of frictions and collisions between solid particles as well as friction between the two-phase flow and tank walls or inside the two-phase flow.

With the increase of the initial particle bed height h, difference comes up. However, difference between cases W8_P5 (Fig. 8) and W8_P7 (Fig. 9) is far less than that between cases W8_P7 (Fig. 9) and W8_P8 (Fig. 10). This may be explained as follows. When the height of solid particle bed is the same as that of the water, which means that the solid particles volume is much more than that of water considering the particle size, momentum loss due to the solid-solid interactions becomes probably much larger than the loss caused by the frictions between solid and water.

In the first 0.3 s, the images shown in Figs. 10 and 11 are very similar although there is not any water in the case W0_P8 while initially all solid particles are immersed in water in the case W8_P8. This may also indicate that the solid-solid interaction has prominent effect on the movement of the case W8_P8. The final steady state of the case W8_P8 has a flat surface while the case W0_P8 shows a different surface shape. This is because of the continuous property of water existing in the case W8_P8 and the discontinuity of the solid particles in the case W0_P8.

The above discussions and comparisons between the five experimental cases indicate that the

solid-solid interactions, *i.e.* frictions and collisions between solid particles, are crucial to the multiphase flow behaviors under the present dam-break experimental conditions.

3.4 Numerical simulations using SIMMER-III

In the present numerical simulations using SIMMER-III, the multiphase flow behaviors in the dam-break experiments were modeled as a three-phase flow with the air, water and solid particles. As discussed in the previous study,[12] the numerical simulations of the liquid dominant multiphase flows, the particle jamming model did not show significant influence on SIMMER-III results. This is because the effect of solid particles is not evident on the flow behaviors. Although in the dam-break experiments, as discussed in the above section, the solid phase has very prominent influence on the multiphase flow behaviors, it was found that the particle viscosity model coupled viscous diffusion term did not contribute to the improvement of numerical simulations. Therefore, in the followings, based on the mass Eq. (2-1) and the momentum Eq. (2-4), the sensitivity of the particle jamming model will be tested and discussed.

3.4.1 Simulation geometry for the experiments

An X-Z two-dimensional Cartesian coordination is adopted for simulating the dam-break experiments. Fig. 12 is a schematic view of the analytical geometry used for SIMMER-III simulations. A same computational cell system is adopted for all dam-break flow cases. In order to obtain an easy application of the same cell system to all experimental cases with various particle bed heights, the first 128 mm in the Z direction is uniformly divided into 8 computational cells whilst the first 64 mm in the X direction is separated into 4 ones with a consideration of the particle size. Since computational cells in the X direction will be counted to obtain XD, the distance between the left wall and the flow front head as defined in Fig. 6, totally 22 cells are defined in the X direction while the Z direction has 19 cells.

SIMMER-III cannot model the pulling out process of the dam board directly by its velocity so that in the simulation, the dam board was assumed to be 19 separated walls in consistence with the computational cell number in the Z direction. By this way, the pulling out of the whole dam board with a vertical speed of 3 m/s can be simulated in such a way that the 19 separated walls are taken away one by one from the bottom to the top in a period of around 86 ms. The cell number in the Z direction of the water particles mixture region lies on the solid particles bed height h. The left, right and bottom wall of the water tank is defined as no-slip wall boundaries. Top boundary of the simulation region is open to the atmosphere and has a continuous inflow-outflow condition under the atmospheric pressure.

3.4.2 Simulation of the reference case with only water

Fig. 13 shows the variation of XD with time in the reference case W8_P0. Simulated results are defined in such a way that for computational cells of the first row in the Z direction, if the volume fraction of water in a cell is no less than 0.3 then its total length in the X direction contributes to XD. As described in Fig. 6, after the experiment started, water arrives at the right wall of the water tank for the first time in 175 ms, the results simulated by SIMMER-III well represent the displacement process of the dam-break flow front head along the bottom of the water tank.

Fig. 14 shows the dam-break flow images during the first period of 2 seconds. First, it should be admitted that SIMMER-III, an Eulerian code using coarse meshes, cannot simulate free surface and water splashing shown in the experimental images. Simulated images of 1.2, 1.6 and 2.0 s seem underestimate the water height along the right or left wall of the water tank. However, experimental images at these instances show that the volume of the splashing water at the front of the flow is very few. On the other hand, considering errors existing in the experimental images as explained in Fig. 5, and the wide range of the volume fraction shown by the color bar, it becomes understandable that there is difficulty for the contour images with coarse mesh cells to clearly present splashing water volumes in the front of the flow. Except for these errors and the limitation of the Eulerian code itself, the simulated results agree well with its experimental counterparts particularly in the general movement trend.

3.4.3 Simulation of experimental cases with a particle-water mixture

As explained in Chapter 2, the particle jamming model of SIMMER-III is represented by Eq. (2-6) in which the maximum volume fraction of solid particles $\alpha_{PJ\max}$ and the index C_{PJ} are two key parameters. So far, 0.7 is defined as the maximum limitation of $\alpha_{PJ\max}$. In order to ensure solid particles volume fraction of one computational cell not to exceed $\alpha_{PJ\max}$, C_{PJ} is defined as – 10 helping to decrease solid particles velocity in its upwind neighbor cells to a very small value quickly and in turn making solid particles in these neighbor cells not able to enter this computational cell, where the volume fraction of solid particles is already close to $\alpha_{PJ\max}\ \beta_{PJ}$, as sketched in Fig. 2.

Simulations of the dam-break experiments, which show significant influence of solid particles on the multiphase flow behaviors, was performed for verification of the particle jamming model. At first, effect of the key parameters $\alpha_{PJ\max}$ and C_{PJ} of the model was tested.

(a) Parametric test of the particle jamming model

Under the current dam-break experimental conditions, experimental images observed did not show that the packing of the solid particles became more compact compared to its initial state after experiments started. Besides, the solid particles used are not compressible, therefore, the solid particles volume fraction in most of the computational cells will probably not exceed initial solid particles volume fractions in the region with solid particles immersed in water. The initial solid particle volume fraction is defined as 0.6 according to experimental measurement. Therefore the possible maximum solid particles volume fraction may be far less than defined $\alpha_{PJ\max}$. Considering this possible difference between the real maximum volume fraction and defined $\alpha_{PJ\max}$, a test simulation of the case W8_P5 was performed by SIMMER-III without application of the particle jamming model.

Fig. 15 shows the test simulation result. Contour images of the solid particles volume distribution of the case W8_P5 at time instants 0.05, 0.1, 0.15, 0.2, 0.25, 0.29s are presented. Each color bar, which shows the range of the solid particles volume fractions from minimum to maximum of the corresponding contour image at each time instant, is automatically obtained by a post-processing tool for SIMMER-III. Fig. 15 clearly shows that the maximum value of the particle volume fraction of the case W8_P5 is around 0.6. Therefore, in those experimental cases, the particle jamming model will have no influence on the

simulation results with a definition of $\alpha_{PJ\max}$ being 0.7.

Figs. 16 to 18 show comparisons between experimental and simulated variation of XD with time in the cases W8_P5, W8_P7 and W8_P8, respectively. In those figures, experimental results are presented together with results simulated by the particle jamming model applied SIMMER-III with various values of parameters $\alpha_{PJ\max}$ (APJ) and C_{PJ} (CPJ). The simulated curves of XD of all these figures are obtained in the same way as that defined for the reference case W8_P0, although the total volume fraction of water plus that of solid particles, instead of the volume fraction of only water, is used here.

Figs. 16 to 18 show that when $\alpha_{PJ\max}$ is defined as 0.7, the simulated XDs arrive at the maximum values faster than their corresponding experimental results. This is because, as expected and explained before, under this definition of $\alpha_{PJ\max}$, the particle jamming model has no influence on the simulations. Therefore, the effect of solid-solid interactions is completely out of consideration and resistance to the dam-break flow as well as the momentum loss is underestimated which leads to a fast flow speed.

Besides, Figs. 16 to 18 show that when $\alpha_{PJ\max}$ is redefined as 0.6 but the parameter C_{PJ} is kept being – 10, the simulated XD arrives at its maximum value much later than its corresponding experimental counterparts. This is because in this case, the particle jamming model function ϕ equals to 0.1^{-10}, when the solid particles volume fraction approaches $\alpha_{PJ\max}\ \beta_{PJ}$. With this value of ϕ, the momentum loss is very large and the velocity of solid particles calculated from the momentum Eq. (2-4) becomes very small, which, in turn, causes the delay of the arrival of the flow front head to the right wall of the water tank.

When 0.6 for $\alpha_{PJ\max}$ and – 1.5 for C_{PJ} are used for the particle jamming model in SIMMER-III, obtained numerical results represent their corresponding experimental results best. When a small absolute value of C_{PJ} is used, the actually effect of the particle jamming model is changed from its original idea. However, by introducing a suitable function ϕ to the K_{qs} in the momentum equation, the frictions between solid particles can be countered to some extent, and then good agreement can be obtained between the experiments and simulated results with adjustment of the model parameters.

(b) Simulation of the dam-break flows

Based on the parameters test results of the particle jamming model, simulation of the dam-break flow processes of all the three cases was performed with $\alpha_{PJ\max}$ = 0.6 and C_{PJ} = – 1.5. For the cases W8_P5 and W8_P7, a period of 2.0 s was simulated while behavior of the case W8_P8 was simulated till 0.8 s because the behaviors shown by images at 2.0 s of the cases W8_P5 and W8_P7 and images at 0.8 s of the case W8_P8 are already close to their final steady state.

Figs. 19 to 21 show comparisons between experimental and simulated images of the dam-break flow behaviors of the cases W8_P8, W8_P7 and W8_P8, respectively. All dam-break flow images represent an area of 260 mm (length) × 208 mm (height). The images labeled “SIMMER-III” are obtained from simulated results of distribution of the total volume fraction of water and solid particles. All those figures show that the simulated flow images over the computation period agree well with their corresponding experimental images. This indicates that, by adjusting the key parameters of particle jamming model,

SIMMER-III can simulate somewhat the interaction, probably mainly frictions, between solid particles under the current dam-break experimental conditions, in which all solid particles are immersed in the liquid working fluid.

3.4.4 Simulation of the experimental case with only particles

Fig. 22 shows the dam-break flow process of the case W0_P8, in which no water exists in the flow. Therefore, it is a gas-solid two-phase flow. All the dam-break flow images represent an area of 260 mm (length) × 208 mm (height). Simulated results show distribution of the volume fraction of solid particles. Although the flow images in the first 0.4 s are very similar to images of the case W8_P8 shown in Fig. 21, which was well simulated, Fig. 22 does not show good agreement between simulated and experimental images for the two analytical cases with different $\alpha_{PJ\max}$ and C_{PJ}.

As discussed before, the maximum solid particles volume fraction of the experiment result probably does not exceed its initial value of 0.6. However, when using SIMMER-III, which treats all solid particles as a continuous fluid and has no special model for interactions between solid particles but a particle jamming model, to simulate the gas-solid two-phase flow, it is of great difficulty.

As shown in Fig. 22, when $\alpha_{PJ\max}$ = 0.6 and a relatively small C_{PJ} are used for simulation, the maximum solid particles volume fractions arrive at unreasonable values as automatically shown by the color bar. This is because when a small C_{PJ} is used, solid particles can still enter into a computational cell even if the volume fraction of solid particles in this cell has already arrived at $\alpha_{PJ\max}$.

On the other hand, when keeping the absolute C_{PJ} being as large as 10, the original idea of the particle jamming model works, in which the velocity of solid particles is artificially decreased in order to keep the maximum volume fractions do not exceed the defined $\alpha_{PJ\max}$. However, under this situation, momentum loss caused by this method is too large that movement of the solid particles is almost stopped as shown in Fig. 22.

The real physical behavior of the case W0_P8 may be as follows. Solid particles in one computational cell can continue to move into its neighbor mesh cells even if the solid particles volume fraction in these neighbor mesh cells has been already at its maximum value, by pushing the solid particles formerly existing in these neighbor mesh cells to move forward. We need to investigate further how to model this kind of pushing force by SIMMER-III.

4 Bubble visualization experiments

4.1 Experimental apparatus and method

Experimental apparatus and method used for the bubble visualization experiments are similar to those for the liquid dominant multiphase flow experiments.[12] The difference lies in the size of the experimental apparatus and the visualization of the bubble inside the particle bed. Fig. 23 is a schematic view of the main experimental dimensions. The main testing section is a cylindrical pool constructed from transparent acrylic resin but with a relatively small size (inner diameter 85 mm and height 395 mm). Different from the apparatus used in the previous study,[12] the cylindrical pool here is directly open to the atmosphere because in these experiments, the liquid height in the cylinder pool will be far from its top exit, which makes it no necessary to have an upper pipe. Inside this cylinder pool, transparent acrylic resin particles (hereafter called acrylic beads) are used to form the particle bed. As the liquid working fluid, sodium iodide (NaI) water solution is used instead of tap water for the purpose of bubble visualization, which will be further explained later.

Outside the cylindrical pool, a quadrate pool made from transparent acrylic resin (length 175 mm, wide 175 mm and height 320 mm) is employed in these experiments for the same purpose of avoiding the convex effect of the cylinder, NaI solution height in the quadrate pool is made the same as that of the corresponding particle beds in the cylindrical pool. The flow road from the hand-made rupture disk to the iron sieve was fabricated with the same radii of 10 mm, therefore, the nominal opening diameter of the rupture disk will be 20 mm. The pressure vessel made from stainless steel, which was sealed by the rupture disk in the beginning of each experiment, has an inner diameter of 35 mm and an effective capacity of about 115 cm^3.

Other characteristics of the experimental apparatus are the same as those of the liquid dominant multiphase pool flow experiments, except that the corresponding dimensions of each part is changed to be consistent with sizes of the new experimental apparatus. All experiments were performed in the same way and the whole experimental system is almost the same as the previous study[12] except that there is only one high-speed camera (400 fps) and one pressure sensor used as shown in Fig. 23 for the bubble visualization experiments.

4.2 Experimental conditions

(a) Physical properties of the NaI water solution

The acrylic beads employed in the experiment have a refraction rate of 1.49. In order to make the bubble passing through the particle bed visible, liquid with the same refraction rate has to be used. NaI water solution[20] and potassium thiocyanate (KSCN) water solution[21] can serve as this kind of working fluid. NaI water solution is employed for our experiments.

The physical properties of the NaI water solution have been measured by many researchers.[22),23] Data of Nishida et al.[23] are adopted in this work since they used the same transparent acrylic resin as our acrylic beads in their experiments. Refraction rate N_D of the NaI water solution is a function of the NaI

concentration C (wt %) in the solution. The following equation shows this mathematic correlation:

$$N_D = 1.2369 + 0.0040486C \quad (4\text{-}1)$$

Accordingly, when the concentration of the NaI water solution is about 64 wt%, the refraction rate of the solution equals to that of the acrylic beads used. In this experiment, therefore, as the liquid working fluid, 64 wt% NaI water solution is used for the purpose of visualization. Besides, sodium thiosulphate ($Na_2S_2O_3$) is added to the NaI solution with a concentration of 0.1 wt% in order to restrain the separation of the I-element from the NaI water solution. The influence of $Na_2S_2O_3$ on the dynamic behavior is ignored in the later SIMMER-III simulation.

Density of the NaI water solution in each experimental case, listed in Table 2, is measured on-site by a gravimeter. The kinematic viscosity ν (m^2/s) of the 64 wt% NaI water solution is a function of the solution temperature T (°C). According to Nishida et al.,[23] when the temperature is in the range of 10 to 40 °C, the temperature-dependent ν is expressed by

$$\nu = (3.18 - 0.0955T + 0.00160T^2 - 9.96 \times 10^{-6} T^3) \times 10^{-6} \quad (4\text{-}2)$$

(b) Initial conditions of each experiment case

The acrylic beads used to form the particle beds have a diameter of 6 mm and a density of 1190 kg/m^3. The NaI water solution with a concentration of 64 wt% has a density close to 1900 kg/m^3. Therefore a low liquid (NaI water solution) height compared to the particle bed height was adopted in each experimental case in order to make the bottom of the particle bed not to leave the bottom of the cylindrical pool and to get a compact particle bed with particles positioned side by side. The initial particle volume fraction in the particle bed area is around 0.57 for all cases. Besides these cases with a particle bed, the reference cases were also performed without particle beds while keeping the liquid heights equal to the particle bed heights of their corresponding cases. Table 2 lists the initial conditions of each case. A relative low initial nitrogen gas pressure around 0.137 MPa was designed for each case. The difference between the initial pressures of each case shown in Table 2 is due to the property of the hand-made rupture disk.

4.3 Experimental results

Pressure transients obtained from the pressure sensor installed at the pressure vessel are presented first. Fig. 24 shows the pressure transient of the reference case 1 and the case I, whilst Fig. 25 shows that of the reference case 3 and the case III. After experiments begin, the pressure in the pressure vessel decreases accompanying the upward expansion of the nitrogen gas.

Because of differences existing in parameters as liquid densities and initial nitrogen gas pressure between the reference cases 1 to 3 and the cases I to III, it is not easy to compare those results between corresponding cases and their reference cases. However, comparison between the reference case 1 and the case I is still possible. Although the case I has a higher initial nitrogen gas pressure than the reference case 1, Fig. 24 shows that the pressure has a longer first expansion period and can arrive at a much lower value in the reference case 1 than in the case I with a acrylic beads particle bed. This is because in the reference

case 1, the resistance received by the nitrogen gas is smaller than that in the case I with a particle bed.

However, liquid height in the reference case 1 is equal to the particle bed height in the case I, and the liquid density is larger than the acrylic beads used in the case I. Therefore, these conditions indicate that in the case I with a particle bed, besides the gravity, interactions between particles as well as those between liquid and solid, and gas and solid contribute much to the resistance received by the nitrogen gas in its expansion process. These interactions between solid particles may also contribute to the difference between pressure transients shown in Fig. 25.

Figs. 26 to 28 show images recorded by the high-speed camera of the corresponding cases. Frames at 10 to 240 ms are presented for a representation of the movement process in each case. The bottom of each frame in these figures corresponds to the location of the iron sieve, which is 10 mm under the bottom of the cylindrical pool as sketched in Fig. 23. All frames in Fig. 26 stand for a region of 85 mm (radial direction) × 130 mm (axial direction) while frames in Figs. 27 and 28 stand for a region of 85 mm (radial direction) × 150 mm (axial direction).

Besides the expansion of the nitrogen gas in the cylindrical pool, Figs. 26 (b) and 27 (b) show the movement of the particles. As can be seen from these figures, first, the particle bed is accelerated to move upward by the expansion of the nitrogen gas, then its velocity decelerates but keeping an upward displacement in the axial direction because of inertia when there is no upward driven force, finally, particles will begin to fall back to the body of the particle bed when the axial velocity decrease to zero as shown by frame at around 100 ms in Figs. 26 (b) and 27 (b).

During this moving process, the particle bed moves as a whole body in the first tens of seconds when the driving force is relatively large, as clearly shown in Fig. 26 (b), part of the particles will separate from the body of the particle bed later. This may probably because the non-uniform collision between particles and the discontinuity of particles as a solid phase. The frame at 80 ms in Fig. 27 (b) also shows a separation between some particles and the body of the particle bed. These figures also show that particles, separating from the body of the particle bed, are mainly those particles, which does not immersed in the NaI water solution in the beginning of the experiment. This is because particles, which are not immersed in the liquid phase, obtained a higher speed than those immersed in the liquid phase since there is no momentum loss caused by the friction between liquid and particles.

Collision between solid particles may have probably contribute to the obvious particle bed movement explained above, because Figs. 26 (a) and 27 (a) do not show such obvious surface change although frames at 80 and 100 ms of Fig. 26 (a) and frames at 80 to 160 ms of Fig. 27 (a) do show some splashing of the NaI water solution at the liquid free surface.

Difference existing in the expansion process of the nitrogen gas between the reference cases and their corresponding cases with a particle bed is shown by Figs. 26 to 28. First, bubble shapes are quite different from each other. Second, difference between the axial velocities of the nitrogen gas can also be seen. Again, because of some parameter differences existing between the reference cases 1 to 3 and the cases I to III, it is of difficulty to clearly conclude which factor determines these differences. However, based on the

comparison and analysis of the pressure transients, the momentum loss due to collisions between solid particles, frictions between liquid-particles, gas-particle and particle-particle, namely, extra resistance to the expansion of the nitrogen gas caused by the existence of the particle bed may have contribute much to these differences.

4.4 Numerical simulations using SIMMER-III

4.4.1 Simulation geometry for the experiments

An R-Z two-dimensional cylindrical geometry is adopted for numerical simulations of the bubble visualization experiments. Similar computational cell systems are used for the cases with particles while some differences exist due to various particles bed and NaI water solution heights among these cases. Fig. 29 is a schematic view of the simulation geometry adopted for the case II listed in Table 2.

4.4.2 Simulation of the reference cases 1 to 3

Figs. 30 to 32 show comparisons between the experimental and simulated pressure transient in the pressure vessel of the reference case 1 to 3, respectively. As can be seen from these three figures, the results simulated by SIMMER-III are close to their corresponding experimental counterparts. Rough comparison between the pressure transients of the three reference cases shows that the pressure oscillating extent in these figures is different from each other. Due to the inertia of the liquid, higher liquid height in the reference case 3 causes longer oscillating period as well as larger amplitude than that of the reference case 1, which has a lowest NaI water solution height among the three reference cases. Meanwhile, the pressure in the pressure vessel of the reference case 1 arrives at its steady state faster than the cases 2 and 3.

Figs. 33 to 35 show comparison between experimental and simulated bubble images of each reference case, respectively. Sizes of the regions presented by these images were labeled in these figures. All radial lengths are equal to the pool diameter. In the Z direction each image begins from the location of the iron sieve shown in Fig. 23, which is 10 mm below the bottom of the cylindrical pool. The tops of these images in Fig. 33 and 34 correspond to the locations of the initial liquid surface, while Fig. 35 shows a total height of 150 mm in the Z direction. Frames at 20 to 180 ms were employed for comparisons. The simulated bubble images are represented by isolines of the nitrogen gas volume fraction in the respective regions.

Fig. 35 shows very good agreement between the experimental and simulated images. Figs. 33 and 34 show that there are some differences between the experimental and simulated images presented in some frames of the reference cases 1 and 2. Both the reference case 1 and 2 have a low liquid height (35 mm and 70 mm, respectively) compared to the cylindrical internal diameter (85 mm), therefore, in order to obtain satisfied images of the bubble in this liquid region, fine mesh system may be necessary. However, SIMMER-III is a code suitable for relatively coarse computational mesh systems. With the increase of the liquid height, this deficiency of SIMMER-III decreases as shown by the good agreement in Fig. 35. Except for these differences, Figs. 33 and 34 show that the simulated images present a general bubble movement trend close to that of the experimental ones.

4.4.3 Simulation of the cases I to III

In the same manner as the simulations of the dam-break experiments, we performed parameter test of $\alpha_{PJ\max}$ (APJ) and C_{PJ} (CPJ) of the particle jamming model at first. Figs. 36 to 38 show the pressure transient in the pressure vessel of the cases I to III, respectively. In these figures, lines labeled "APJ = 0.7_CPJ = – 10" and "APJ = 0.6_CPJ = – 2.5" are the results simulated by SIMMER-III. As can be seen from these figures, when C_{PJ} = – 10, pressure transient of each case is far different from the experimental one. In the cases II (Fig. 37) and III (Fig. 38), when C_{PJ} = – 10, the simulated pressure agrees with the experimental results in the first several milliseconds but in the following period the simulated pressure keeps being a very large value without oscillation. This is because the jamming function is so large that the momentum loss is overestimated and the particle bed cannot move upward, which in turn leads to difficulty for the nitrogen gas in the pressure vessel to expand and go out of the pressure vessel. Although the difference shown in Fig. 36 is not as obvious as that in Figs. 37 and 38, the jamming function is also too large with C_{PJ} = – 10, which causes the expansion extent of the nitrogen gas being underestimated. When a small absolute value is used for C_{PJ}, together with 0.6 for $\alpha_{PJ\max}$, the simulated results of pressure transients show good agreements with their corresponding experimental ones.

Namely, on the basis of the above well-simulated pressure transients in the pressure vessel, which can be seen as the driven force to the mixture of liquid and solid particles in the pool, dynamic behavior of bubbles and particle beds can be obtained and compared. Figs. 39, 41 and 43 show the bubble movement images while Figs. 40, 42 and 44 show the particle bed movement of the corresponding experimental case. The dimensions of each image were labeled in these figures. What need to be pointed out is, in Figs. 39 and 41, the Z direction of each image starts from the location of the iron sieve and ends at the initial height of the particle bed surface equaling to the NaI solution height in the surrounding quadrate pool, which is higher than the initial height of the NaI water solution in the cylindrical pool, that is why the top part of the experimental images is not visible.

Figs. 39, 41 and 43 show there is great difficulty for the simulated bubble images to agree with their corresponding experimental counterparts. Those figures show that the simulated bubbles expand and move faster than their actual situations in the beginning, whilst later because the top particles, which are not initially immersed in the NaI water solution, does not move upward and stays at the initial position, the simulated bubbles have difficulty to continue their upward expansion and movement but separate into 2 small bubbles as shown in Figs. 41 and 43. The dynamic behavior of particle bed was not well represented either as shown by comparisons between experimental and simulated particle bed images, disagreement especially exists in the change of the surface shape of the particle beds shown in Figs. 40 and 42.

According to the analysis of the dam-break experiments, the existence of the particles, which were not immersed in the liquid, cause special difficulty for the SIMMER-III code to correctly simulate the experimental dynamic behavior. Therefore, SIMMER-III cannot provide appropriate simulation on these experiments because of the lack of models, which deal with the interaction between solid-solid particles. Although the pressure transient in the pressure vessel, the driven force, can be well represented by adjusting the particle jamming model, however, additional models need to be introduced to SIMMER-III

for the purpose of simulating the interactions inside or between solid phases as well as controlling the packing fraction of solid phase not to exceed its maximum value.

Solid phase momentum equations defined in some literatures[6),7),10),11),24),25)] are found including a solid stress term with "particle phase viscosity", incorporating the kinetic theory for granular flows,[12),26)] to consider the interaction between solid particles, including collisions and friction etc. Detail descriptions can be referred to the user's manual of FLUENT^{TM} code[27)] and the theory guide of MFIX code.[28)] While Chen et al.,[29)] Lettieri et al.[30),31)] and Cammarata et al.[32)] obtained good simulations by employing a "particle bed model", developed by Foscolo and Gibilaro,[33),34)] in their solid momentum equation to consider the interactions between particles and using an excess solid volume correction algorithm to ensure the maximum solid packing fraction not to become an unreasonable value. It is be necessary to investigate further what kind of models should be introduced, and what kind of numerical techniques should be used to implement the prospective models to the SIMMER-III code.

For the bubble visualization experiments, SIMMER-III cannot either well represent the dynamic behavior of the bubble expansion and also the particle bed, part of which is not initially immersed in the NaI water solution. Additional physical models considering the interactions between solid particles and methods, instead of the particle jamming model, for obtaining a physically reasonable maximum packing fraction of solid particles, might be necessary for SIMMER-III. Both the kinetic theory for granular flows and the particle bed model with an excess solid volume correction algorithm may be worth consideration.

5 Concluding remarks

In this study, two series of experiments, that is dam-break experiments and bubble visualization experiments, were performed to investigate dynamic behaviors of solid-particle dominant multiphase flows. The experiments were intended to simulate multiphase flow behaviors possible in a disrupted LMFR core with low energy level for the purpose of the verification of the models and methods in the SIMMER-III code. Verification of SIMMER-III was also conducted based on numerical analyses of these experimental results. In the present experiments, solid particles have a prominent effect on the dynamic behaviors of multiphase flows because collisions between solid particles as well as frictions between particle-particle, liquid-particle, and gas-particle contribute much to the transient behaviors.

The experimental analyses show that SIMMER-III can simulate the dam-break flow behaviors well, in which all solid particles are immersed in the liquid phase, by adopting suitable values of the key parameters used in the particle jamming model. This means that the particle jamming model represents the motion of solid particles in liquid phase. However, for gas-solid two-phase dam-break flows, currently, SIMMER-III has great difficulty to model the flow behaviors due to the lack of mechanistic models to treat the mechanical interactions among particles, such as friction force and stress force. For the bubble visualization experiments, SIMMER-III cannot either well represent the dynamic behavior of the bubble expansion as well as the movement of the particle bed, part of which is not initially immersed in the NaI water solution. This indicates that the particle jamming model is not effective on simulating the motion of solid particles in gas phase although it can be adjusted to compensate some friction losses. SIMMER-III has to be further improved with suitable models, which can well represent interactions between solid particles and can well model the reasonable maximum packing fraction of solid particles in any computational cell.

For future work, it might be necessary to carefully investigate what kind of model and numerical technique should be implemented to the current SIMMER-III code. A particle bed model developed by Foscolo and Gibilaro with an excess solid volume correction algorithm proposed by Lettieri et al. may be worthy of attentions for its relative simplicity on implementation. Besides, a complete solid stress term incorporating the kinetic theory for granular flows, which have been adopted in some codes including several commercial ones, may also be worth consideration for the improvement of SIMMER-III.

References

1) Kondo, Sa., Tobita, Y., Morita, K., et al., 1992. SIMMER-III: an advanced computer program for LMFBR severe accident analysis. In: Proc. Int. Conf. on Design and Safety of Advanced Nuclear Power Plant (ANP '92), Tokyo, Japan, 25-29 October, pp. 40.5.1-40.5.11.
2) Tobita, Y., Kondo, Sa., Yamano, H., et al., 2000. Current status and application of SIMMER-III, an advanced computer program for LMFR safety analysis. In: Proc. 2nd Japan-Korea Symposium on nuclear Thermal Hydraulics and Safety (NTHAS2), Fukuoka, Japan, 15-18 October, pp. 65-72.
3) Tobita, Y., Momentum Exchange Function Model in SIMMER-III (Research Document), Japan Nuclear Cycle Development Institute, to be published.
4) Russel, W.B., 1983. Effects of interactions between particles and rheology of dispersions, in R.E.Meyer (ed.), Theory of Dispersed Multiphase Flow, Academic Press, New York, pp. 1-34.
5) Horie, H., Shirakawa, N., Tobita, Y., et al., 2001. The effect of bubble size on the radial distribution of void fraction in two-phase flow in a circular tube. Journal of Nuclear Science and Technology 38, pp. 711-720.
6) Gidaspow, D., 1994. Multiphase Flow and Fluidization: Continuum and Kinetic Theory Descriptions. Academic Press, New York.
7) Ding, J. and Gidaspow, D., 1990. A bubbling fluidization model using kinetic theory of granular flow. AIChE Journal 36, pp. 523-538.
8) Tsuji, Y., Kawaguchi, T., Tanaka, T., 1993. Discrete particle simulation of two-dimensional fluidized bed. Power Technology 77, pp. 79-87.
9) Gera, D., Gautam, M., Tsuji, Y., et al., 1998. Computer simulation of bubbles in large-particle fluidized beds. Power Technology 98, pp. 38-47.
10) Boemer, A., Qi, H. and Renz, U., 1997. Eulerian simulation of bubble formation at a jet in a two-dimensional fluidized bed. Int. J. Multiphase Flow 23, pp. 927-944.
11) Taghipour, F., Ellis, N., and Wong, C., 2005. Experimental and computational study of gas-solid fluidized bed hydrodynamics. Chemical Engineering Science 60, pp. 6875-6867.
12) Morita, K., Liu, P., Matsumoto, T., et al., 2007. Fundamental study on flow characteristics of disrupted core pool at a low energy level, JAEA-Research 2007-032.
13) Lun, C.K.K., Savage, S.B., Jeffery, D.J., et al., 1984. Kinetic theories for granular flow: inelastic particles in Couette flow and slightly inelastic particles in a general flow field. J. Fluid Mech. 140, pp. 223-256.
14) Yamano, H., Fujita, S., Tobita, Y., et al., 2003. SIMMER-III: a computer program for LMFR core disruptive accident analysis -Version 3.A model summary and program description. Japan Nuclear Cycle Development Institute, JNC TN9400 2003-071.
15) Ishii, M. and Zuber, N., 1979. Drag coefficient and relative velocity in bubbly, droplet or particulate flows. AIChE Journal 25, pp. 843-855.
16) Tobita, Y., Morita, K., Kondo, Sa., et al., 1991. Interfacial area modeling for a multiphase, multi-component fluid-dynamics code. In: Proc. Int. Conf. on Multiphase Flows, Tsukuba, Japan, 24-27 September, pp. 361-364.

17) Saunders, F.L., 1961. Rheological properties of monodisperse latex systems I. Concentration dependence of relative viscosity. Journal of Colloid Science, 16, 13.
18) Krieger, I.M., 1972. Rheology of monodisperse lattices. Advances in Colloid and Interface Science, 3, 111.
19) Bohl, W.R. and Luck, L.B., 1990. SIMMER-II: a computer program for LMFBR disrupted core analysis. Los Alamos National Laboratory, LA-11415-MS.
20) Baldwin, J.T., Deutsh, S., Geseloitts, D.B., Tarbell, J.M., 1994. LDA measurement of mean velocity and Reynolds stress fields within an artificial heart ventricle. J. Biomech. Eng, 116, pp. 190-200.
21) Schoephoerster, R.T., Chandran, K.B., 1991. Velocity and turbulence measurements past mitral valve prosthese in a model left ventricle. J. Biomechanics 24, pp. 549-562.
22) Matsui, G., Monji, H., Sakakibara, J., et al., 1999. Study on thermal-hydraulic phenomena in porous media. Japan Nuclear Cycle Development Institute, JNC TY9400 99-005. (in Japanese)
23) M. Nishida, T. Yamane, Asztalos, B., 1998. “Enshin ketsueki pump nai nagare nokasika teiryou kaiseki,” Kikai gijyutsukennkyuujyo syohou 52 [3], pp. 74-92. (in Japanese)
24) Li, S., Ding, Y., Wen, D., etc., 2006. Modelling of the behavior of gas-solid two-phase mixtures flowing through packed beds. Chemical Engineering Science 61, pp. 1922-1931.
25) Makkawi, Y., and Ocone, R., 2005. Modelling the particle stress at the dilute-intermediate-dense flow regimes: a review. KONA No.23, pp. 49-63.
26) Jenkins, J.T., and Savage, S.B., 1982. A theory for the rapid flow of identical, smooth, nearly elastic, spherical particles. J. Fluid Mech. 130, pp. 187-202.
27) Fluent User’s Manual, 1996. Fluent, Inc., Lebanon, New Hampshire, USA.
28) Syamlal, M., Rogers, W., and O’Brien, T.J., 1993. MFIX document: theory guide. Technical Note, DOE/METC-04/1004, NTIS/DE94000087, National Technical Information Service, Springfield, Virginia, USA.
29) Chen, Z., Gibilaro, L.G. and Foscolo, P.U., 1999. Two-dimensional voidage waves in fluidized beds. Ind. Eng. Chem. Res. 38 [3], pp. 610-620.
30) Lettieri, P., Brandani, S., Yates, J.G., et al., 2001. A generalization of the Foscolo and Gibilaro particle-bed model to predict the fluid bed stability of some fresh FCC catalysts at elevated temperatures. Chem. Eng. Sci. 56, pp. 5401-5412.
31) Lettieri, P., Cammarata, L., Micale, G., et al., 2003. CFD simulations of gas fluidized beds using alternative Eulerian-Eulerian modeling approaches. International Journal of Chemical Reactor Engineering 1, A5.
32) Cammarata, L., Lettieri, P., Micale, G., et al., 2003. 2D and 3D CFD simulations of bubbling fluidized beds using Eulerian-Eulerian models. International Journal of Chemical Reactor Engineering 1, A48.
33) Foscolo, P.U. and Gibilaro, L., 1987. Fluid dynamic stability of fluidized suspensions: the particle bed model. Chem. Eng. Sci. 42 [6], pp. 1489-1500.
34) Gibilaro, L., 2001. Fluidization dynamics, Butterworth Heinemann, London.

Nomenclature

$A_{qq'}$	viscous term for $K_{qq'}$
$B_{qq'}$	turbulent term for $K_{qq'}$
C_{PJ}	parameter of the particle jamming model
g	gravitational acceleration (m/s^2)
$K_{qq'}$	momentum exchange function between velocity components q and q'
K_{qs}	momentum exchange function between velocity component q and structure
P	pressure (Pa)
S	strain rate (m/s)
t	time (s)
v	velocity (m/s)
VM_q	virtual mass term (kg/(m^2 s^2))

Greek letters

α	volume fraction
α_{MP}	maximum volume fraction of solid particles defined in the particle viscosity model
$\alpha_{PJ\max}$	maximum packing volume fraction of solid phases defined in the particle jamming model
β_{PJ}	fraction of $\alpha_{PJ\max}$ above which the particle jamming model is applied
ϕ	function of the particle jamming model
μ	viscosity (Pa s)
μ_C	effective viscosity of the continuous liquid phase
μ_L	viscosity of the continuous liquid phase
ν	kinematic viscosity (m^2/s)
$\bar{\rho}$	macroscopic density (kg/m^3)
υ	specific volume (m^3/kg)

Subscripts

L	liquid phase
P	solid particles
q, q'	velocity component of the three fluid phases

Table 1: Initial conditions of the dam-break experiments.

Cases	Water height (H mm)	Particle bed height (h mm)	The ratio of H/h
W8_P0 (Reference case)	128	0	8/0
W8_P5	128	80	8/5
W8_P7	128	112	8/7
W8_P8	128	128	8/8
W0_P8	0	128	0/8

Table 2: Initial conditions of the bubble visualization experiments.

	Reference case 1	Reference case 2	Reference case 3	Case I	Case II	Case III
Particle bed height (mm)	0	0	0	50	100	230
Liquid height (mm)	50	100	230	35	70	140
Density of the NaI water solution (kg/m^3)	1890	1890	1870	1895	1905	1885
Initial pressure of the nitrogen gas (MPa)	0.133	0.135	0.139	0.135	0.137	0.137

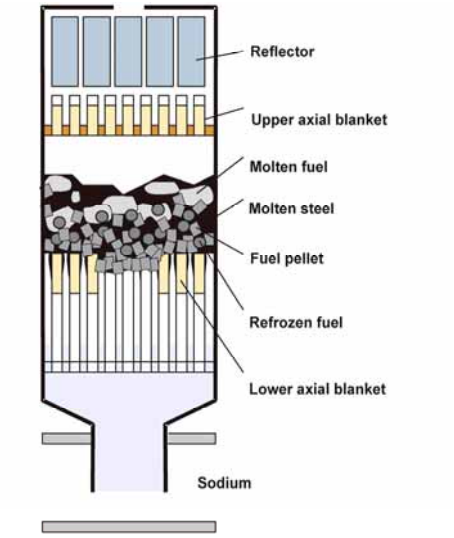

Fig. 1: Schematic view of a disrupted core with subassembly scale.

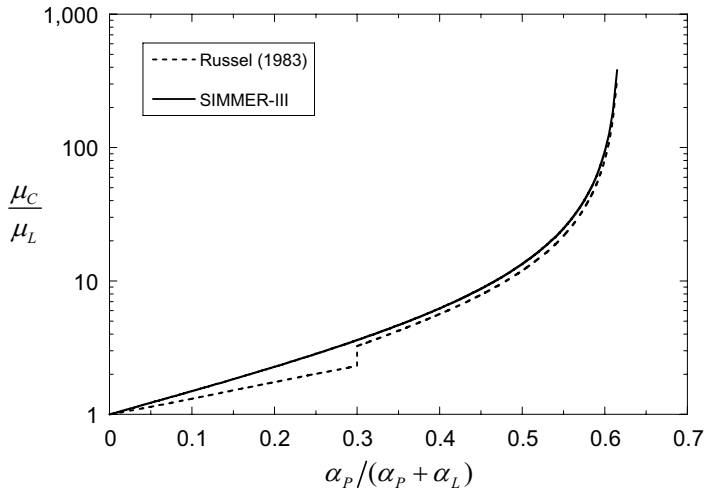

Fig. 2: Increase of effective viscosity due to existence of solid particles.

μ_C is the effective viscosity of the continuous liquid phase while μ_L is the viscosity of the continuous liquid phase. α_P and α_L is the volume fraction of solid-particle and liquid phases, respectively.

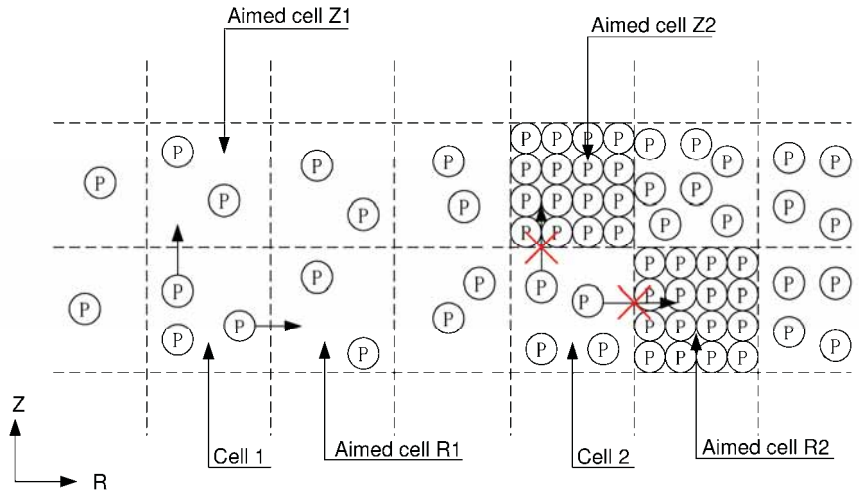

Fig. 3: Schematic view of particle jamming phenomenon.

"P" means particle. Particles in cell 1 can enter into the aimed cells R1 and Z1 because the particle volume fraction in cells R1 and Z1 is less than its maximum while particles in cell 2 cannot enter into the aimed cells R2 and Z2 because the particle volume fraction in cells R2 and Z2 is in its maximum.

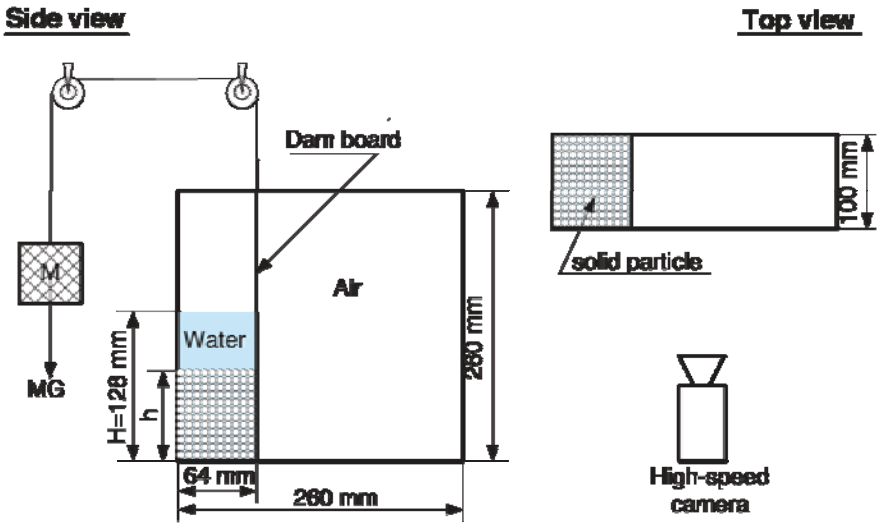

Fig. 4: Schematic view of the dam-break experimental apparatus.

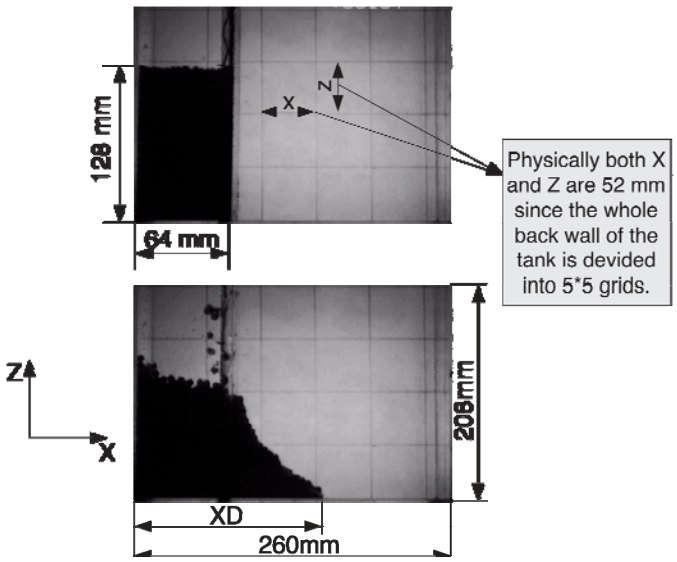

Fig. 5: View of image error and definition of XD.

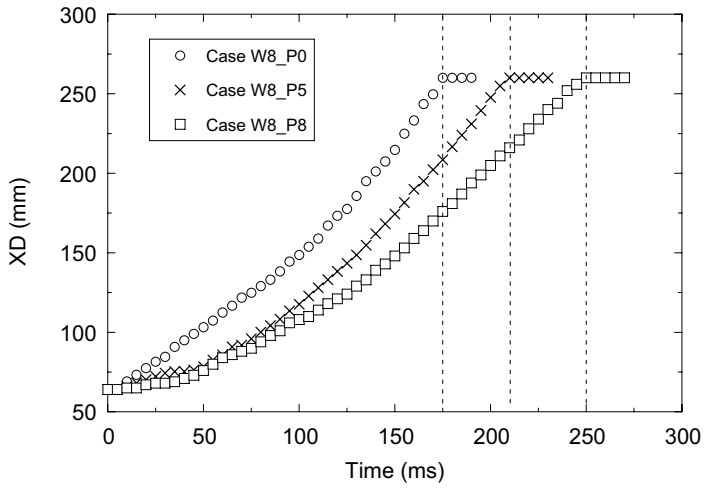

Cases	W8_P0	W8_P5	W8_P7	W8_P8	W0_P8
DT (ms)	175	210	225	250	260

Fig. 6: Comparison of the dam-break flow speeds along the bottom of the water tank.

DT is defined as the time that takes the flow front heads to arrive at the right wall of the tank, i.e. the front head of the flow of the cases W8_P0, W8_P5, W8_P7, W8_P8 and W0_P8 arrives at the right wall of the water tank at 175 ms, 210 ms, 225 ms, 250 ms and 260 ms, respectively.

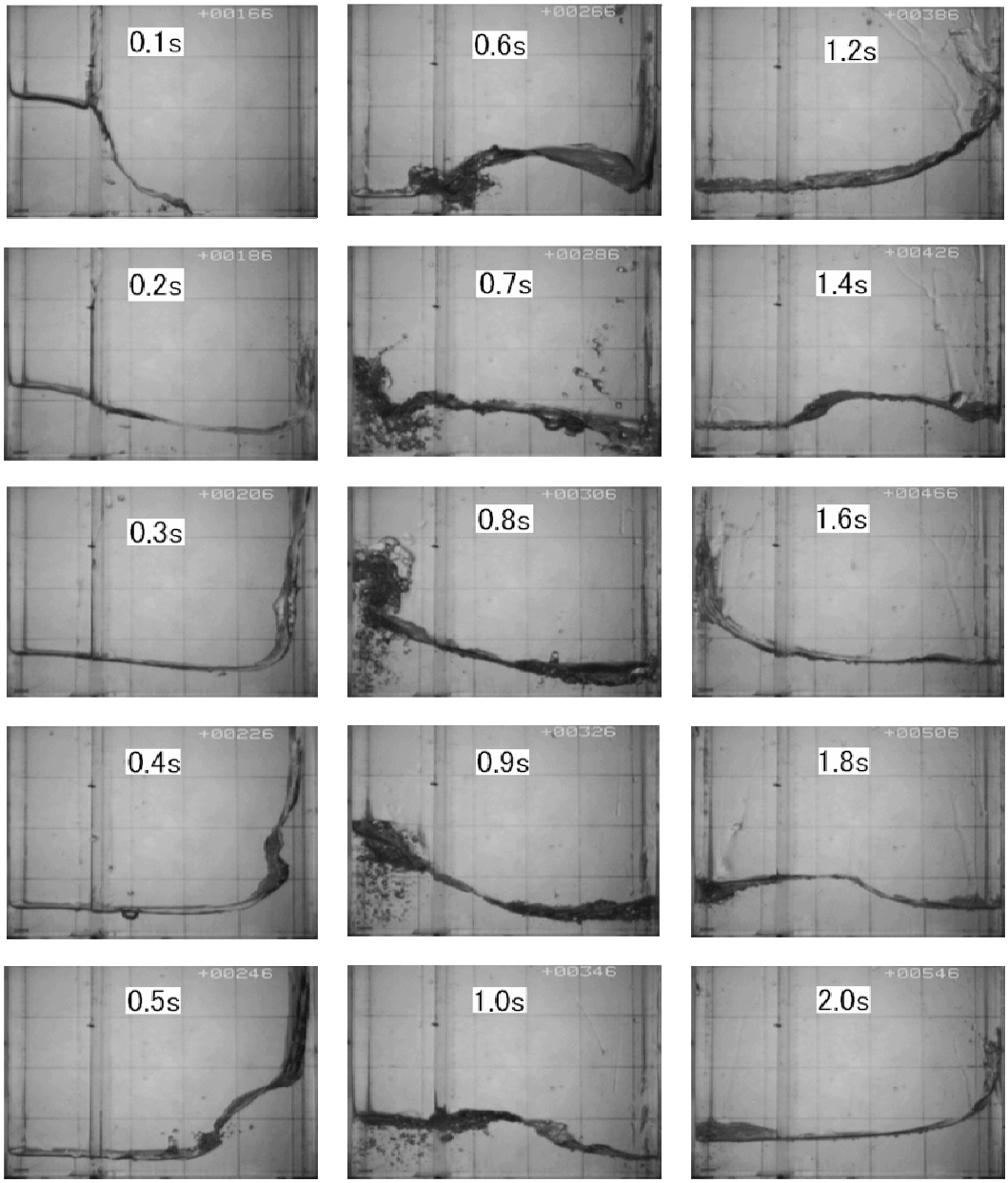

Fig. 7: Dam-break flow images of the case W8_P0 (h = 0 mm; H = 128 mm).

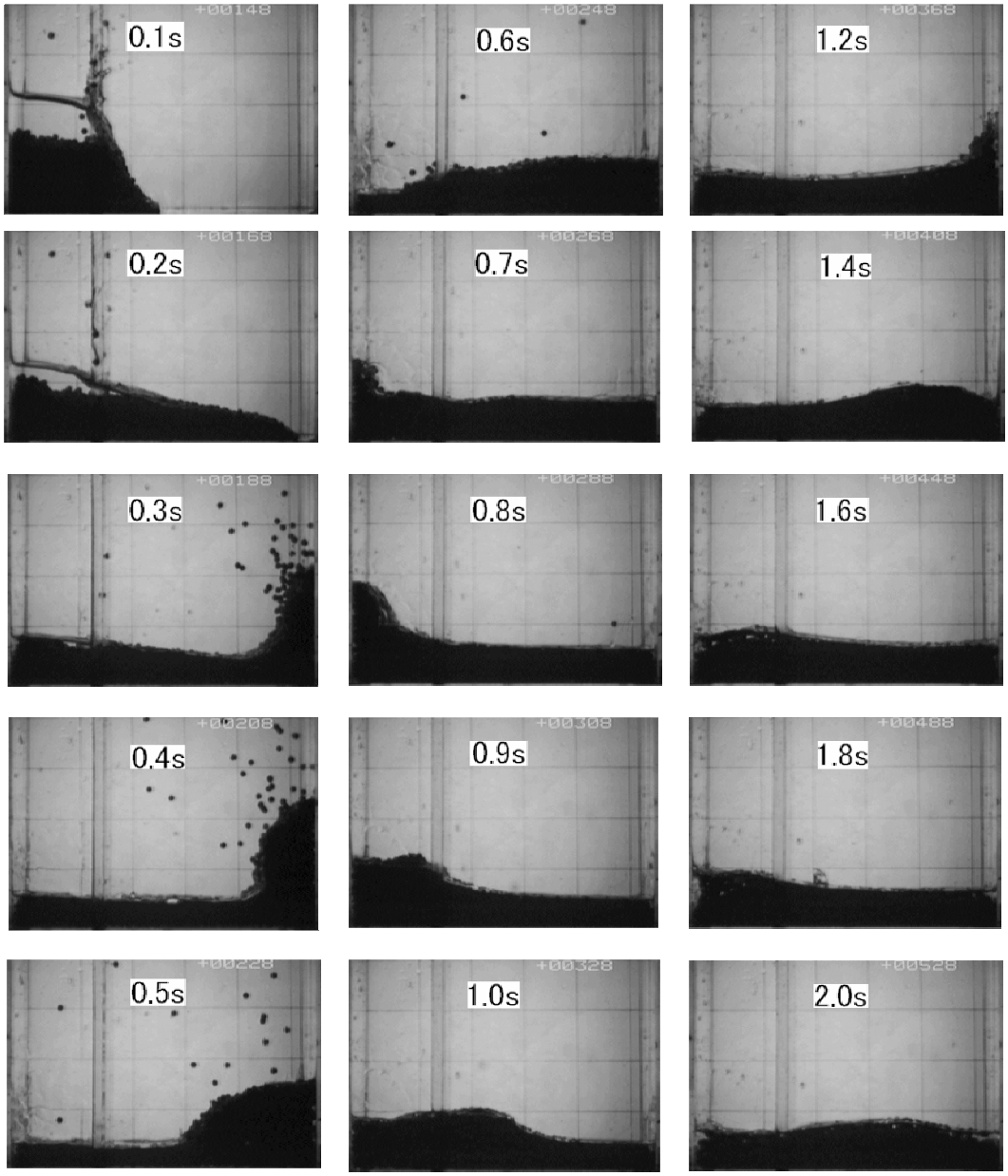

Fig. 8: Dam-break flow images of the case W8_P5 (h = 80 mm; H = 128 mm).

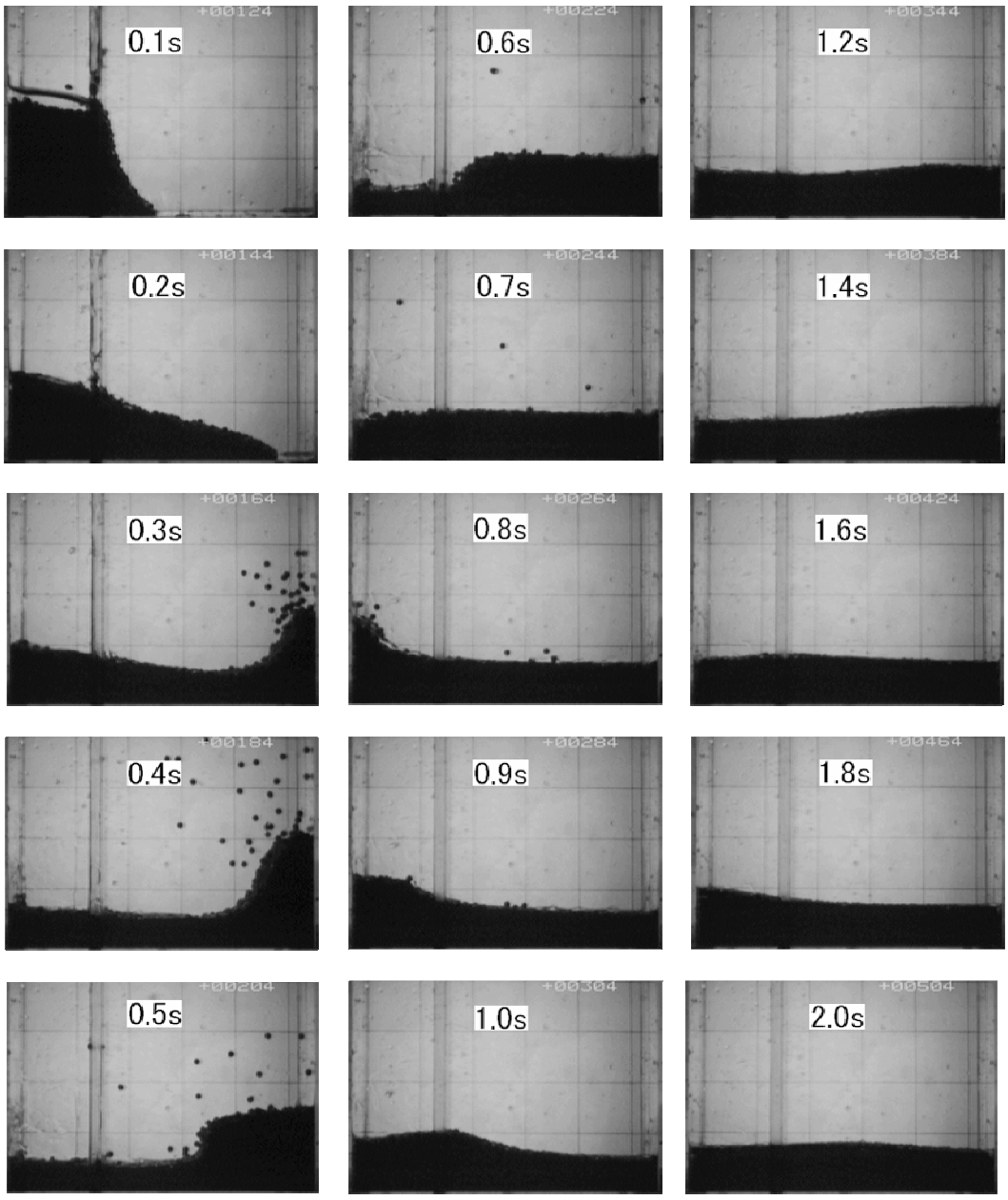

Fig. 9: Dam-break flow images of the case W8_P7 (h = 112 mm; H = 128 mm).

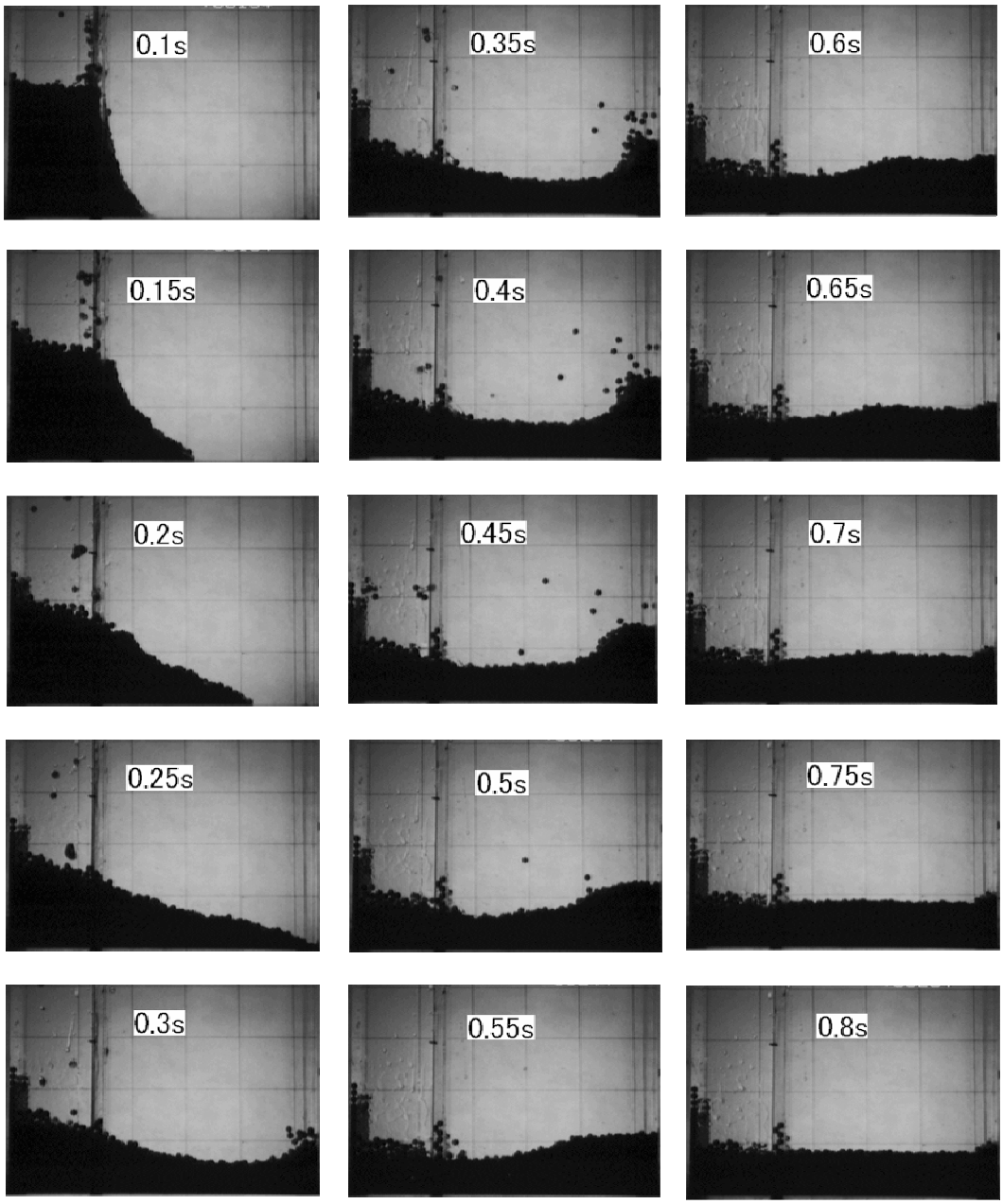

Fig. 10: Dam-break flow images of the case W8_P8 (h = 128 mm; H = 128 mm).

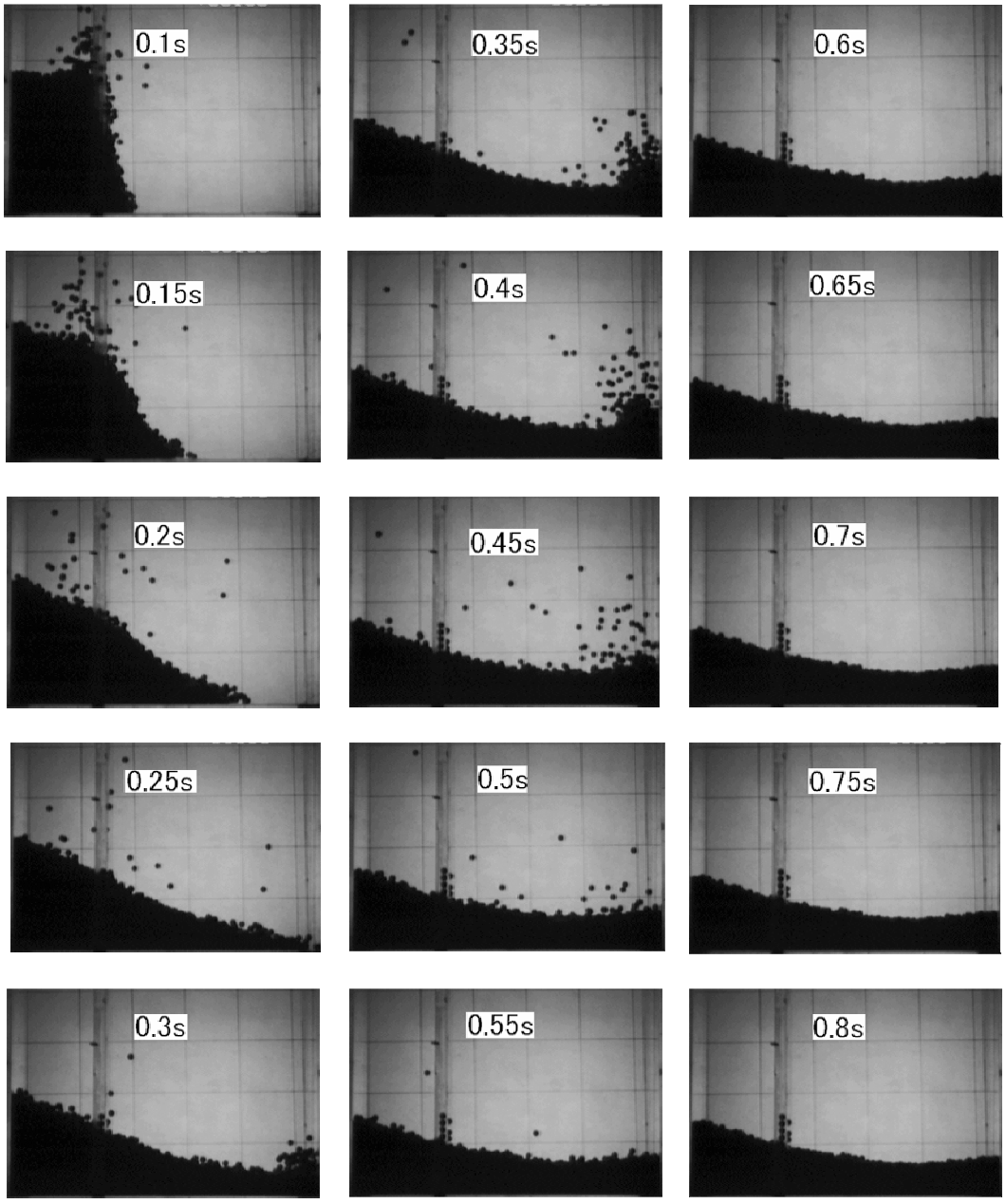

Fig. 11: Dam-break flow images of the case W0_P8 (h = 128 mm; H = 0 mm).

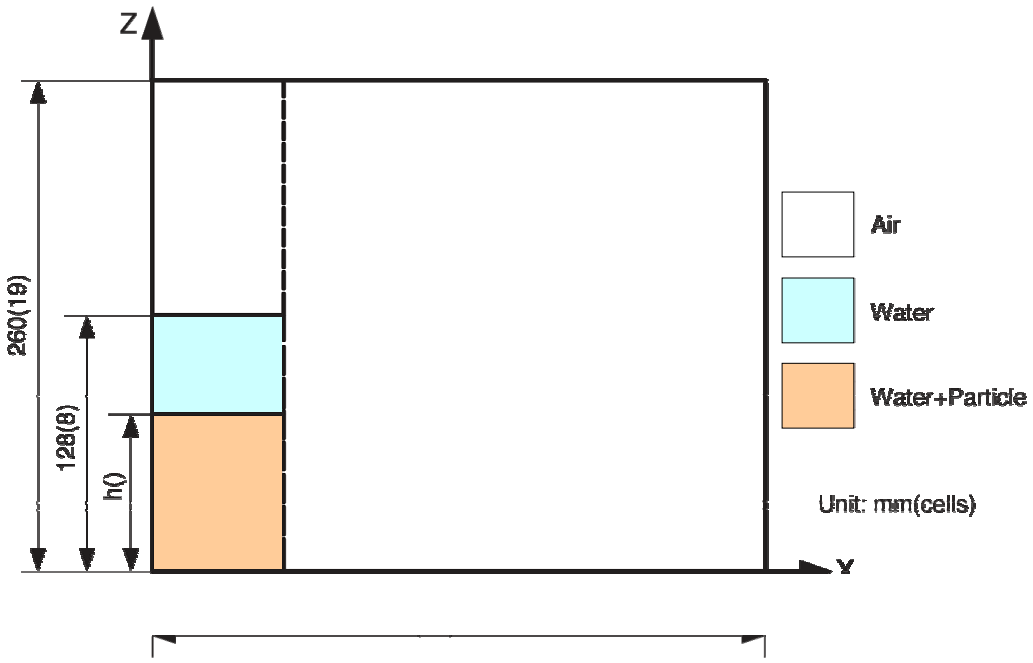

Fig. 12: Analytical geometry for SIMMER-III simulation.

The dam board was separated to 19 parts according to the mesh cell size in the vertical Z direction. The mesh cell size for the water + particle area is depended on the particle bed height h.

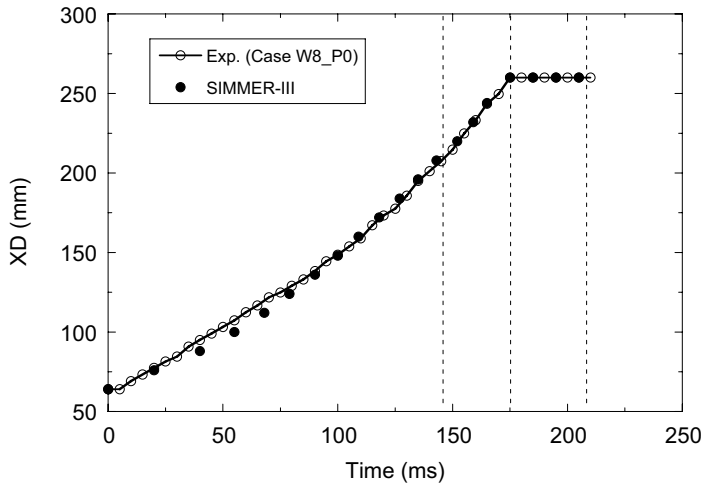

Fig. 13: Variation of XD with Time in the reference case W8_P0.

XD is the distance between the left wall and the front head of the dam-break flow as defined in Fig. 5.

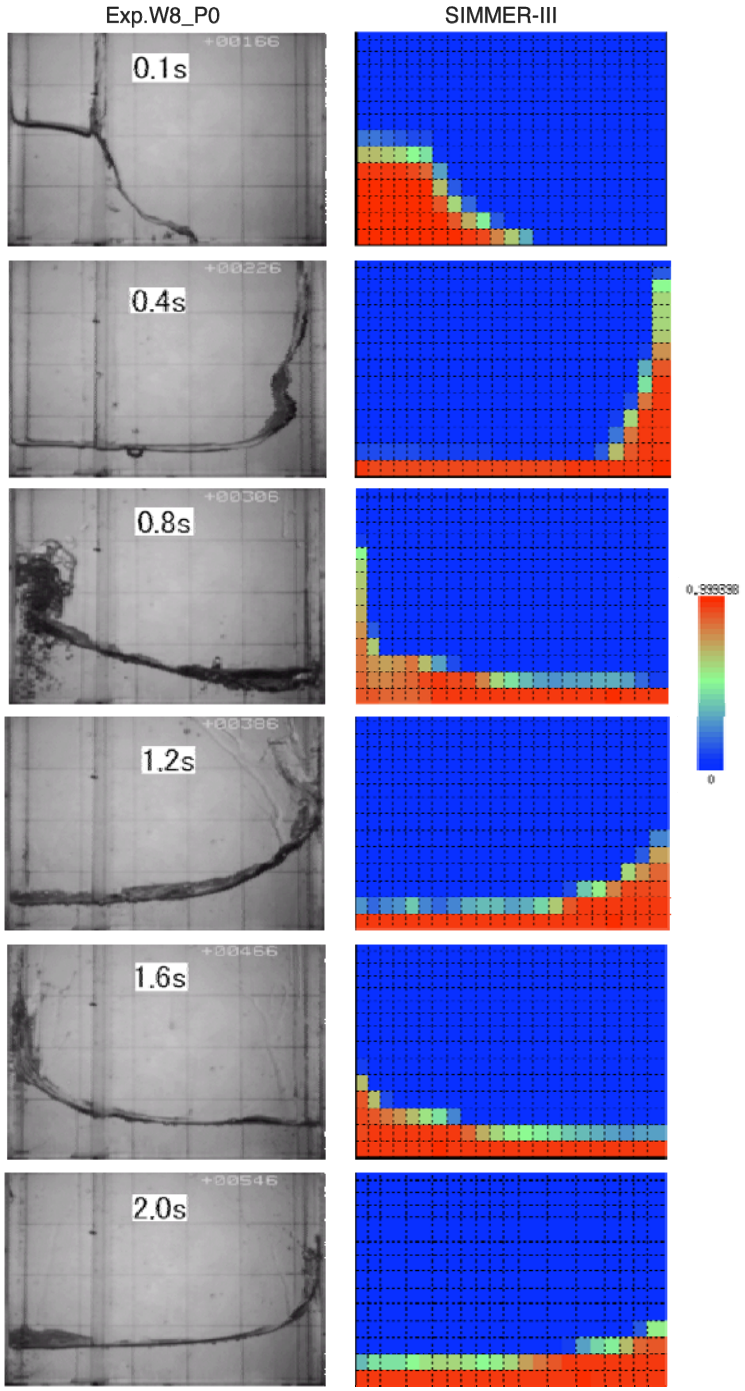

Fig. 14: Dam-break flow images of the reference case W8_P0.

All images represent a region of 260 mm (length) × 208 mm (height). The color bar shows the volume fraction of water in the SIMMER-III simulation results.

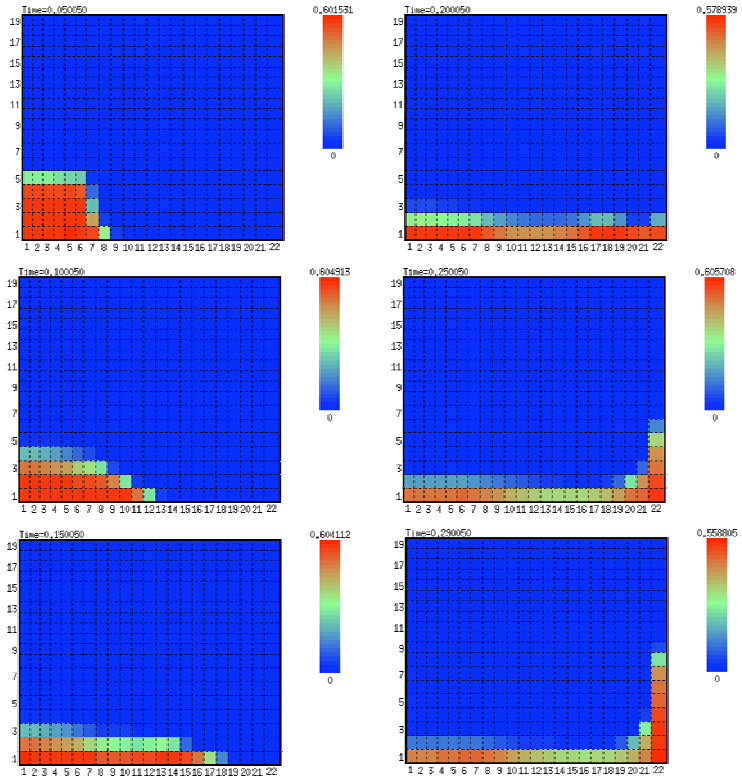

Fig. 15: Sample images of simulated solid particles distribution in the case W8_P5.

All images represent a region of 260 mm (length) × 208 mm (height). The SIMMER-III simulation was performed without the particle jamming model. The color bars show the volume fraction of solid particles in the SIMMER-III simulation results.

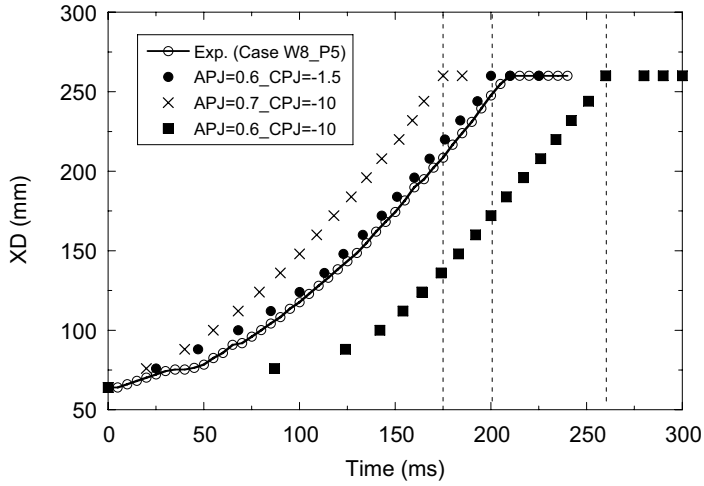

Fig. 16: Comparisons of XD between experimental and simulated variation in the case W8_P5.

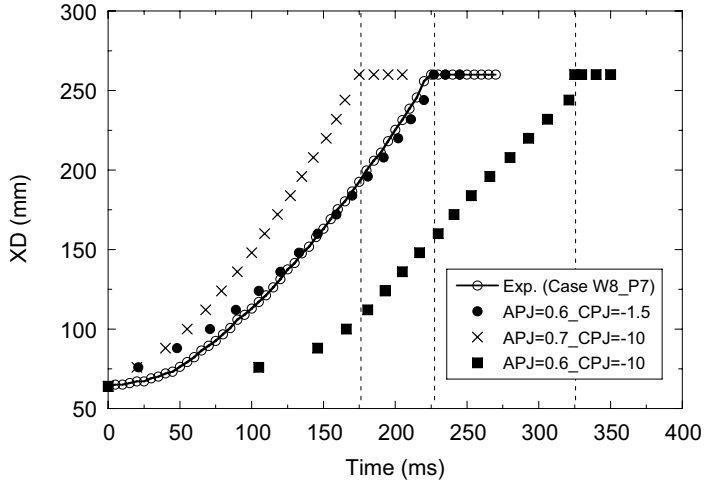

Fig. 17: Comparisons of XD between experimental and simulated variation in the case W8_P7.

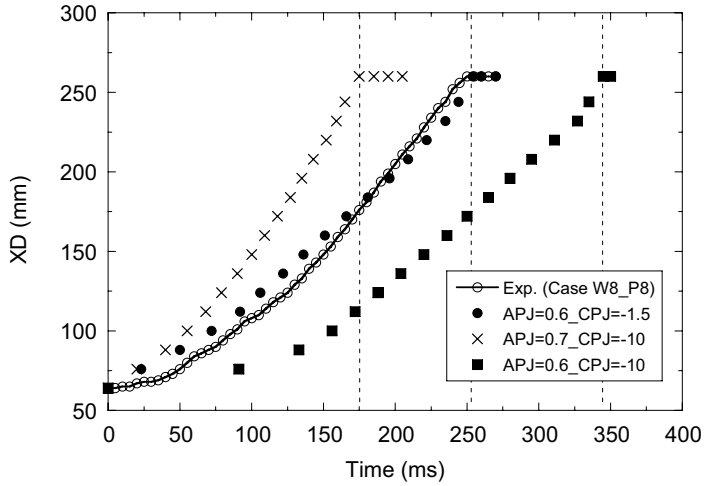

Fig. 18: Comparisons of XD between experimental and simulated variation in the case W8_P8.

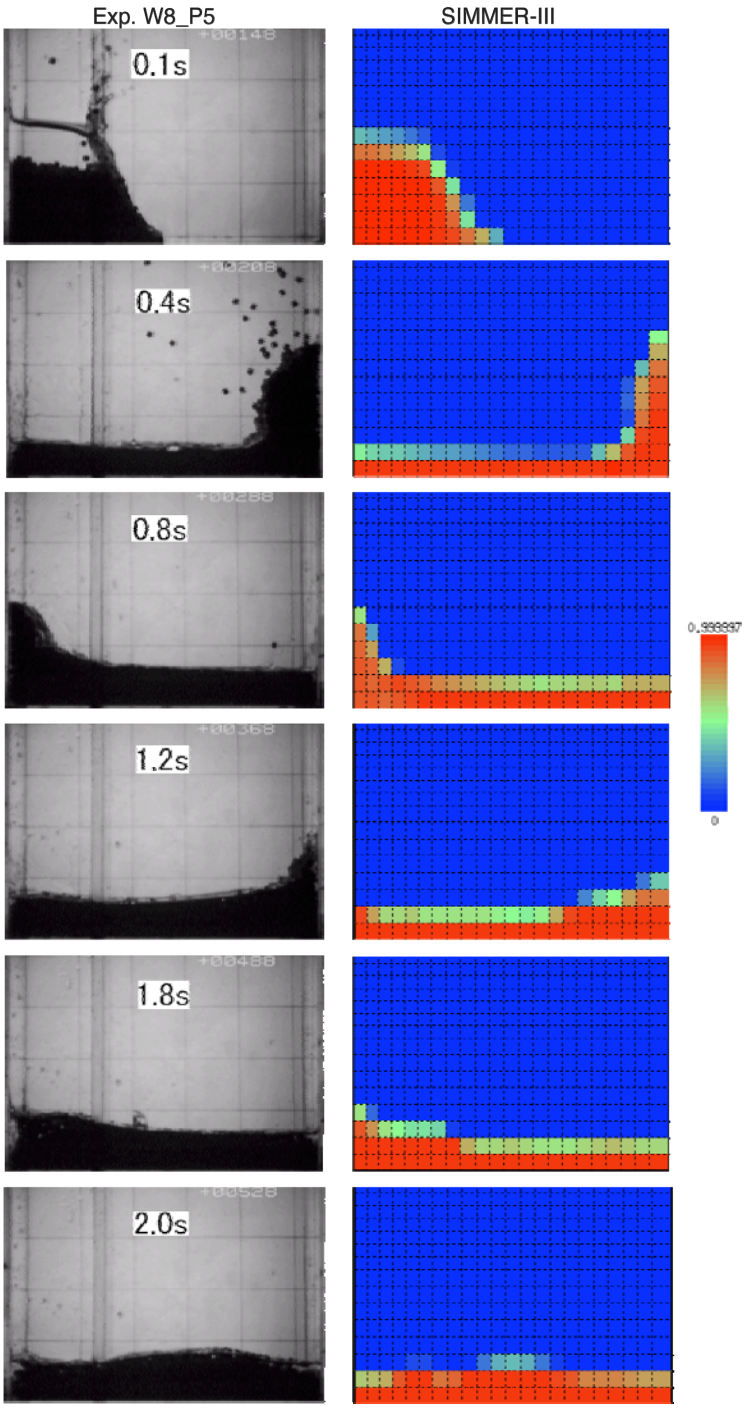

Fig. 19: Dam-break flow images in the case W8_P5.

All images represent a region of 260 mm (length) × 208 mm (height). The color bar shows the total volume fraction of water and solid particles in the SIMMER-III simulation results.

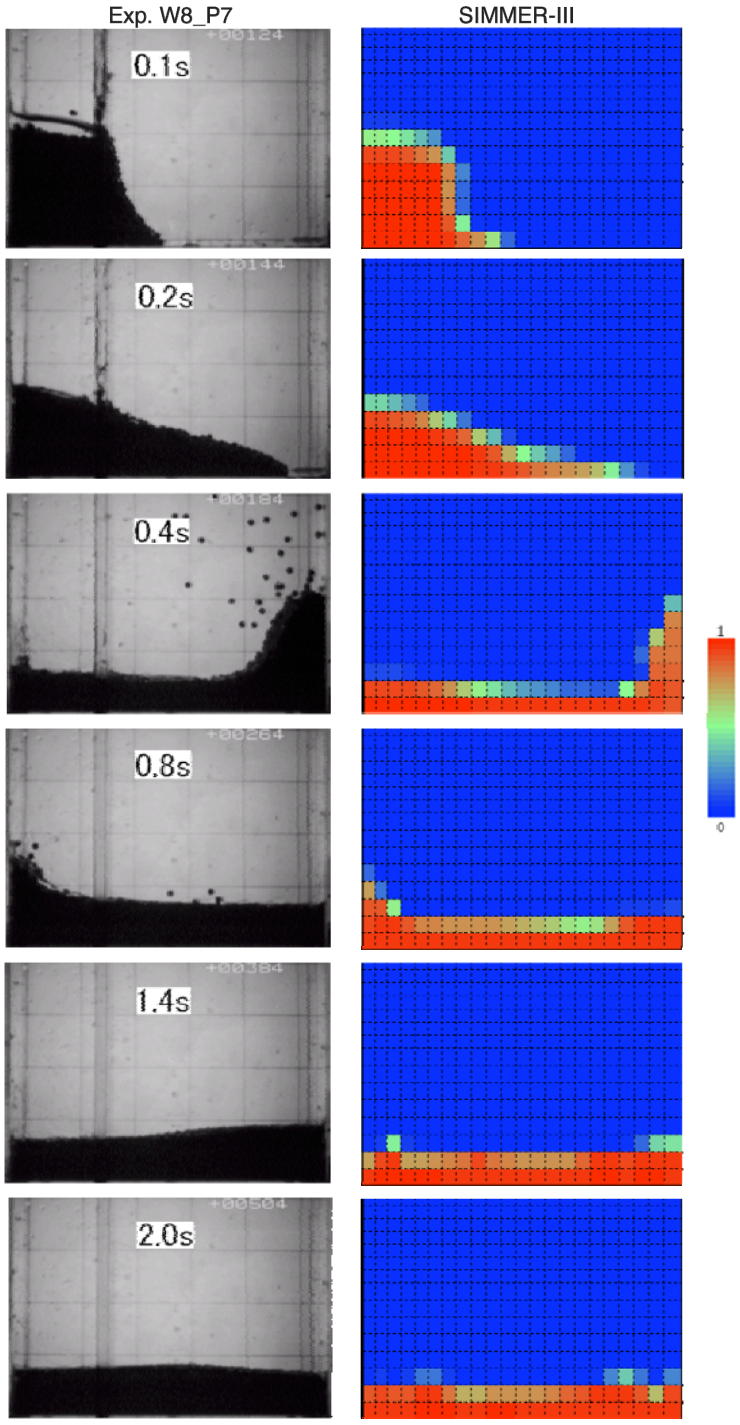

Fig. 20: Dam-break flow images in the case W8_P7.

All images represent a region of 260 mm (length) × 208 mm (height). The color bar shows the total volume fraction of water and solid particles in the SIMMER-III simulation results.

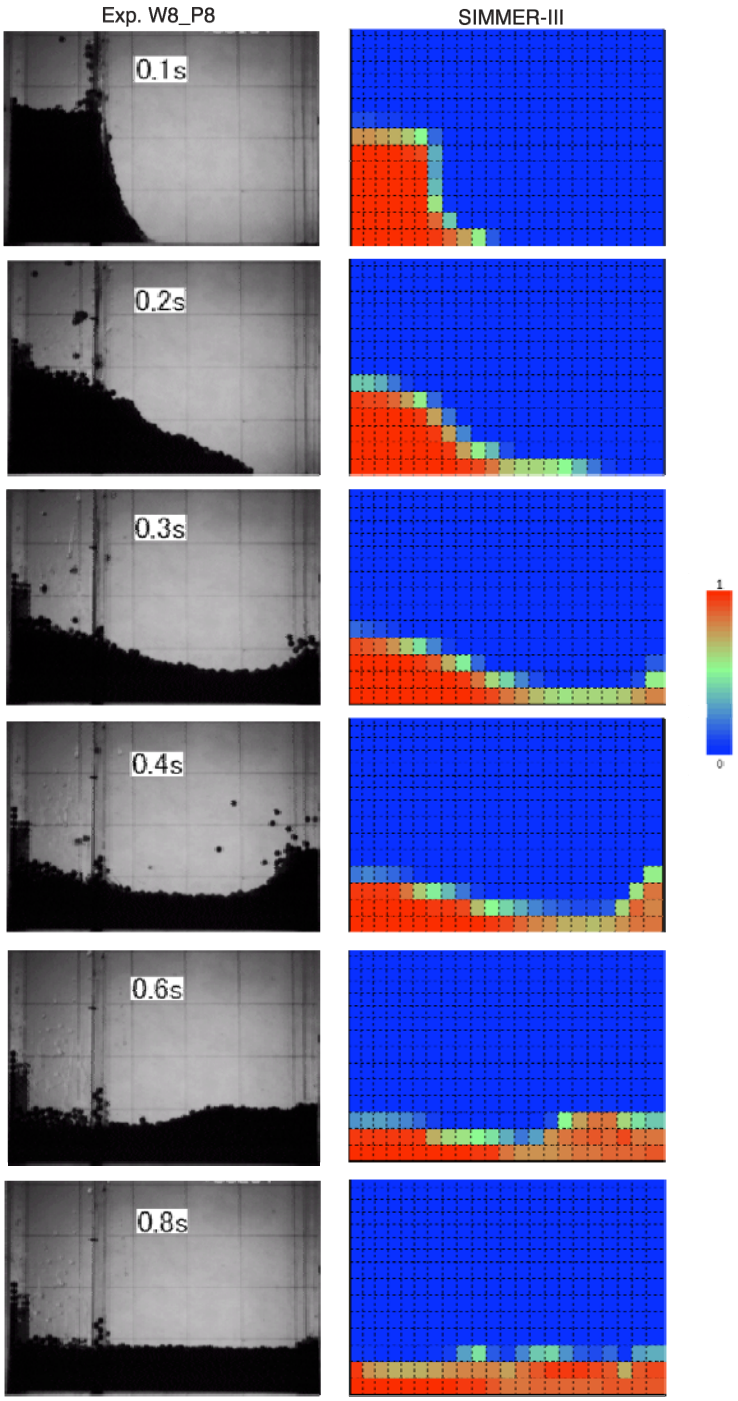

Fig. 21: Dam-break flow images in the case W8_P8.

All images represent a region of 260 mm (length) × 208 mm (height). The color bar shows the total volume fraction of water and solid particles in the SIMMER-III simulation results.

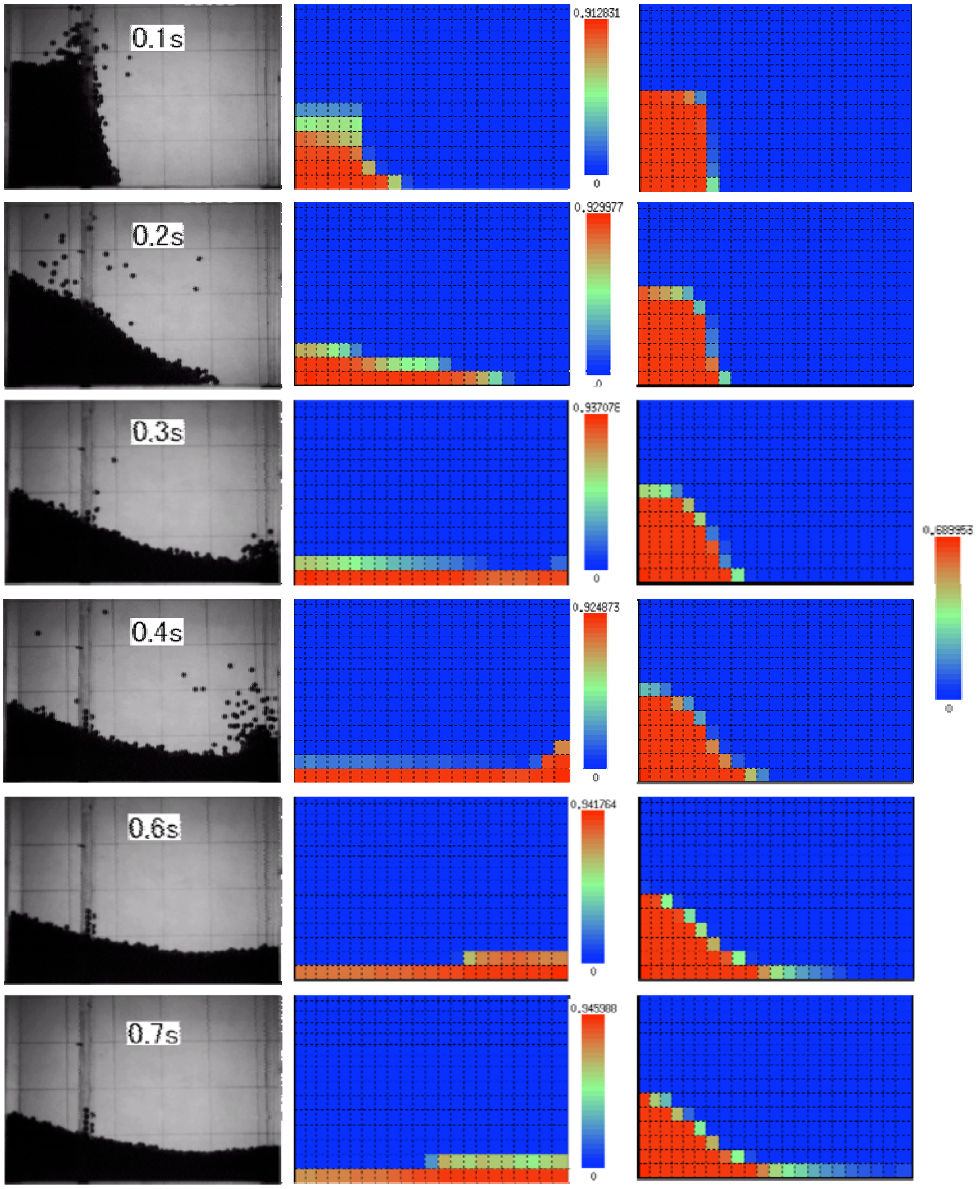

Fig. 22: Dam-break flow images in the case W0_P8.

All images represent a region of 260 mm (length) × 208 mm (height). The color bar shows the volume fraction of solid particles in the SIMMER-III simulation results. The simulation results labeled "SIMMER-III APJ = 0.6, CPJ = − 0.6" and "SIMMER-III APJ = 0.7, CPJ = − 10" are obtained with $\alpha_{PJ\max} = 0.6$, $C_{PJ} = -0.6$ and $\alpha_{PJ\max} = 0.7$, $C_{PJ} = -10$, respectively.

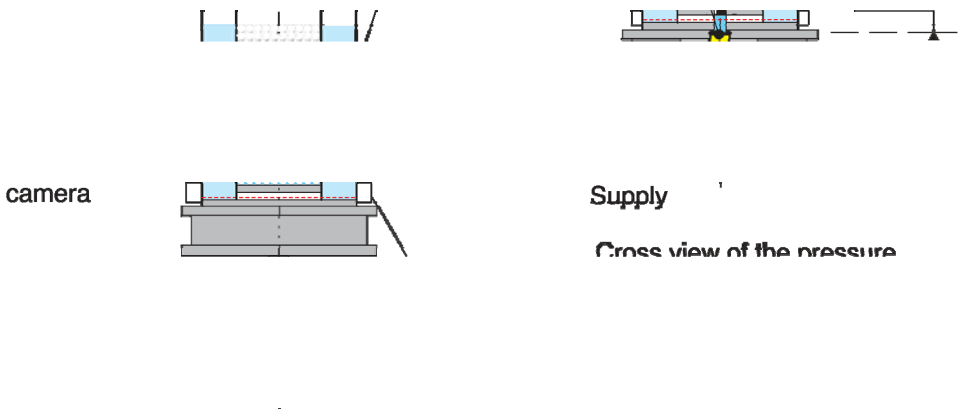

Fig. 23: Schematic view of the bubble visualization experiment apparatus.

Inside the cylindrical pool, part of the particles is in the air while the left is immersed in the NaI water solution. In real experimental situations, particles immersed in the NaI water solution cannot be viewed but the movement of the nitrogen gas becomes visible in this area.

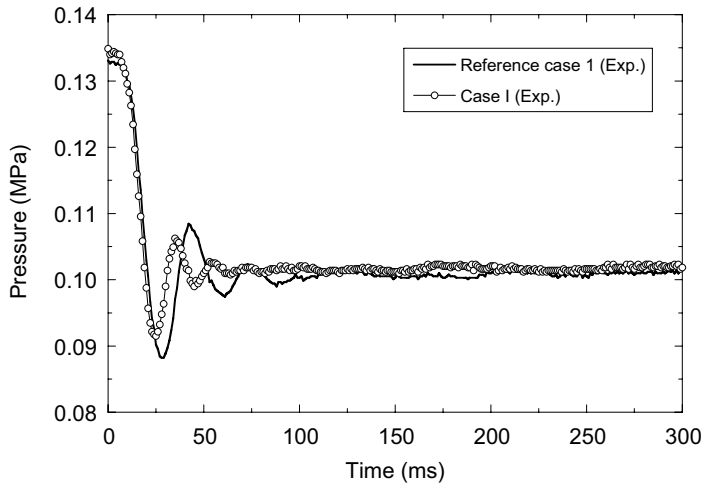

Fig. 24: Pressure transient in the pressure vessel of the reference case 1 and case I.

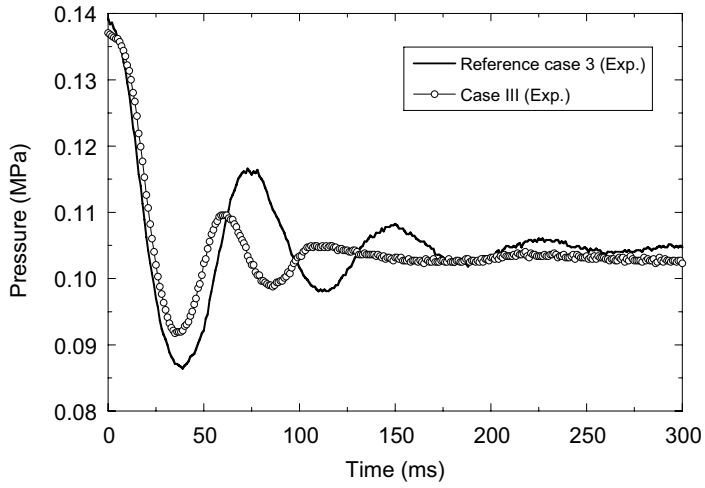

Fig. 25: Pressure transient in the pressure vessel of the reference case 3 and the case III.

Fig. 26: Images of the reference case 1 and the case I.

(a) Images of the reference case 1 with a 50 mm liquid height

(b) Images of the case II with a 35 mm liquid height and a 50 mm particle bed

The index (1) refers to the liquid surface in the surrounding quadrate liquid pool, equaling to the initial liquid surface height in the cylindrical pool. The index (2) refers to the liquid surface in the surrounding quadrate liquid pool, equaling to the initial particle bed height in the cylindrical pool. The index (3) refers to the liquid surface in the cylindrical pool. The symbol d means the axial distance between (2) and (3).

All images represent the same area of 85 mm (cylindrical pool diameter, radial direction) × 130 mm (axial direction).

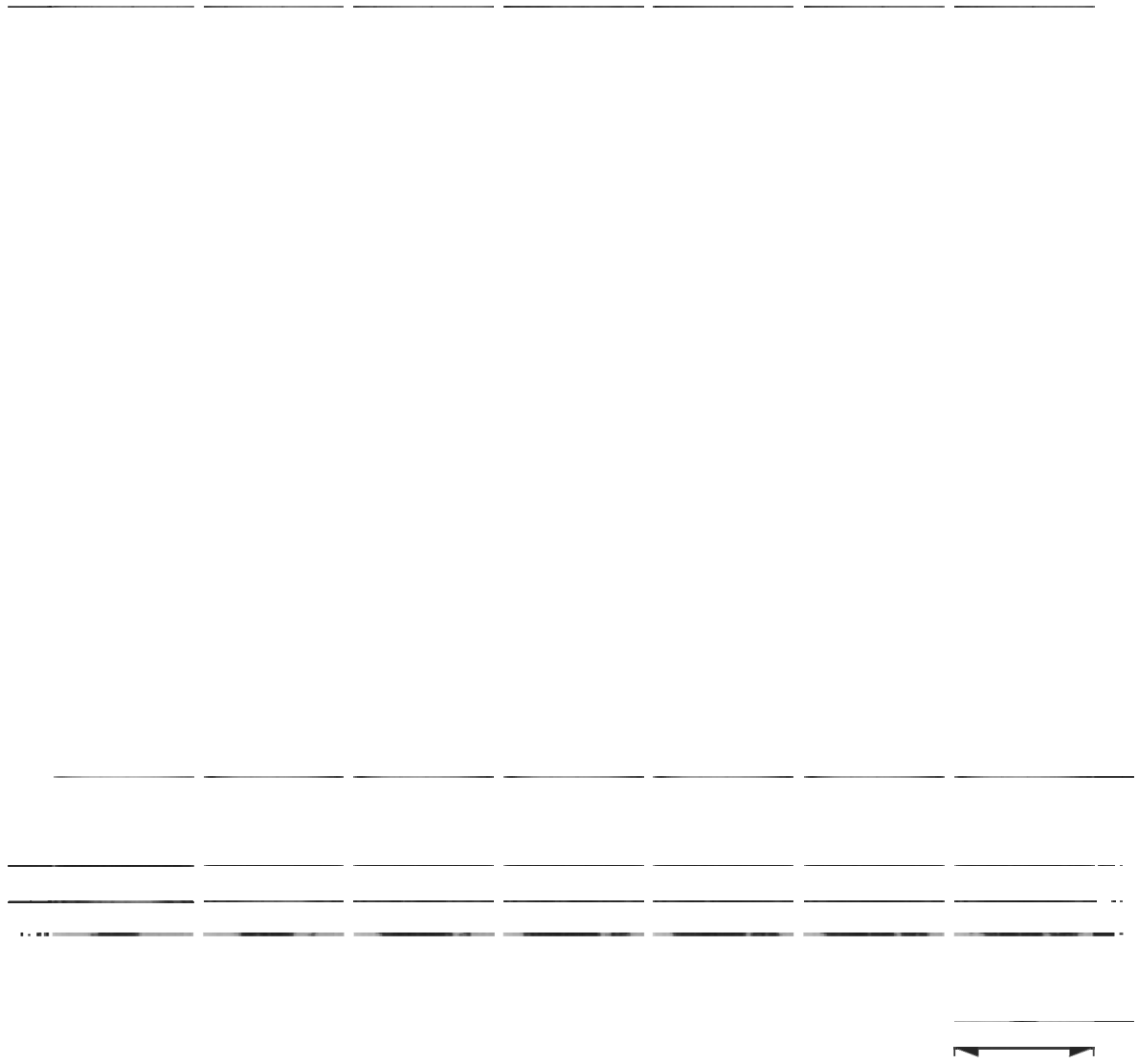

Fig. 27: Images of the reference case 2 and the case II.

(a) Images of the reference case 2 with a 100 mm liquid height

(b) Images of the case II with a 70 mm liquid height and a 100 mm particle bed

The index (1) refers to the liquid surface in the surrounding quadrate liquid pool, equaling to the initial liquid surface height in the cylindrical pool. The index (2) refers to the liquid surface in the surrounding quadrate liquid pool, equaling to the initial particle bed height in the cylindrical pool. The index (3) refers to the liquid surface in the cylindrical pool. The symbol d means the axial distance between (2) and (3).

All images represent the same area of 85 mm (cylindrical pool diameter, radial direction) × 150 mm (axial direction).

Fig. 28: Bubble images of the reference case 3 and the case III.

(a) Images of the reference case 3 with a 230 mm liquid height

(b) Images of the case II with a 140 mm liquid height and a 230 mm particle bed

All images represent the same area of 85 mm (cylindrical pool diameter, radial direction) × 150 mm (axial direction).

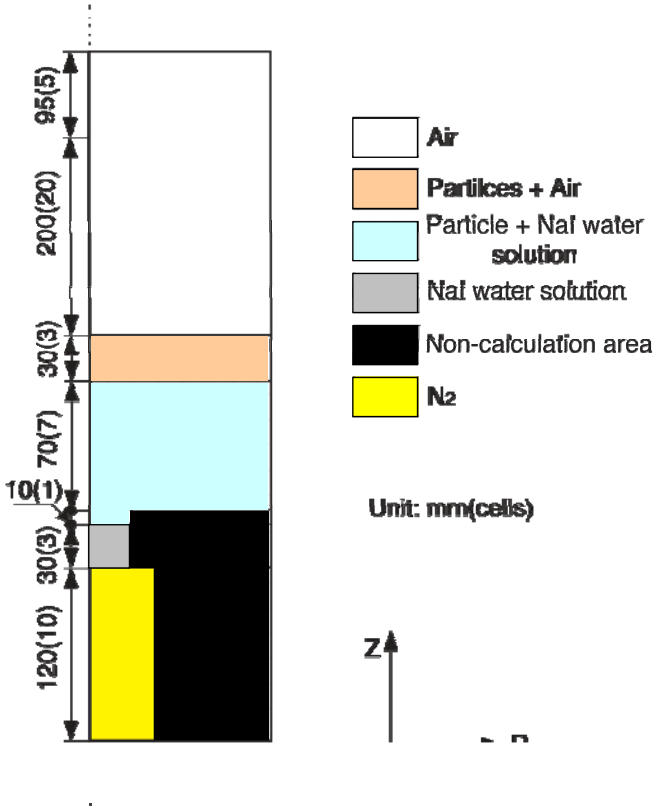

Fig. 29: Simulation geometry for the bubble visualization experiments.

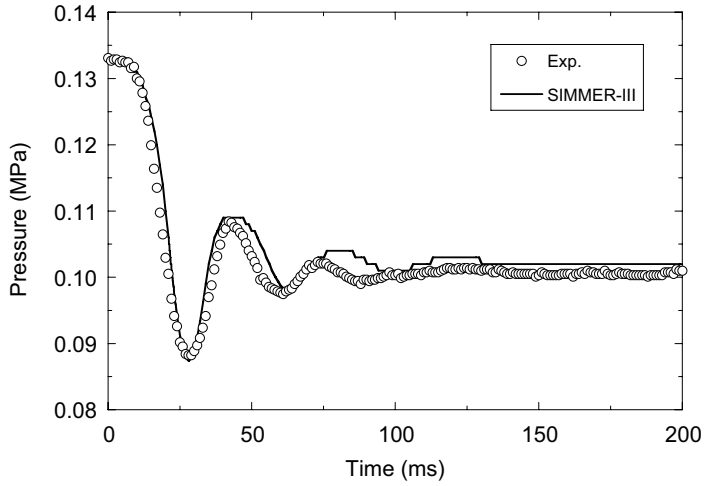

Fig. 30: Pressure transient in the pressure vessel of the reference case 1.

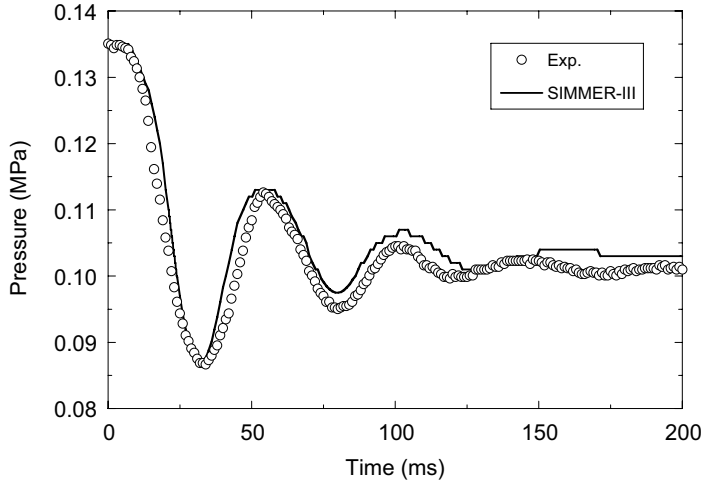

Fig. 31: Pressure transient in the pressure vessel of the reference case 2.

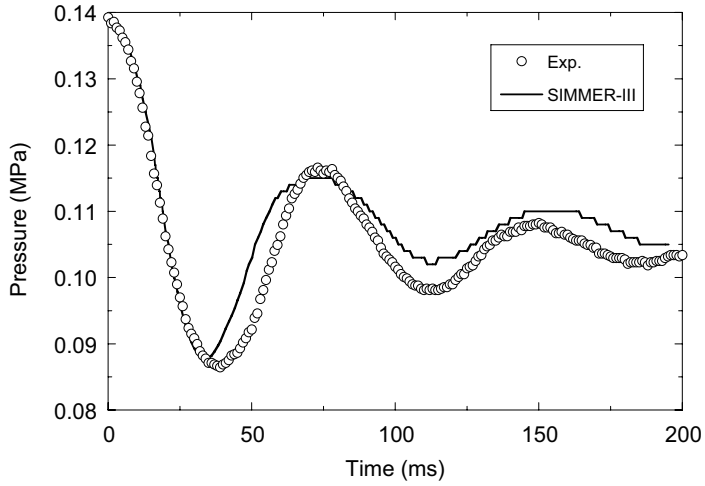

Fig. 32: Pressure transient in the pressure vessel of the reference case 3.

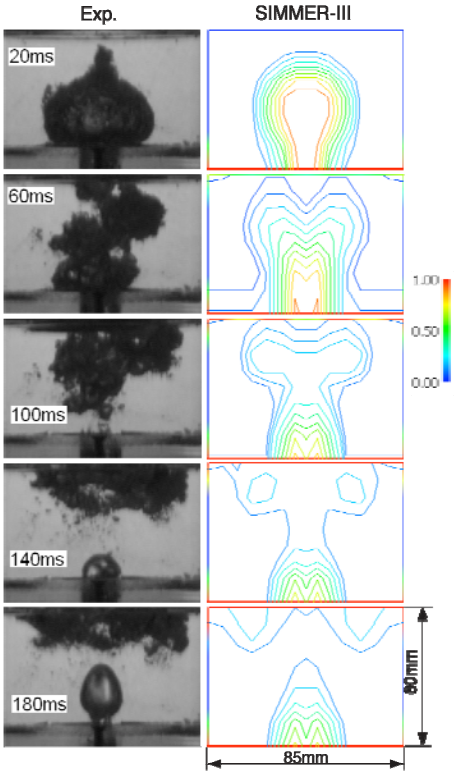

Fig. 33: Comparison between experimental and simulated bubble images of the reference case 1.

The color bar shows the vapor volume fraction of the contour lines.

Fig. 34: Comparison between experimental and simulated bubble images of the reference case 2.

The color bar shows the vapor volume fraction of the contour lines in the SIMMER-III simulation results.

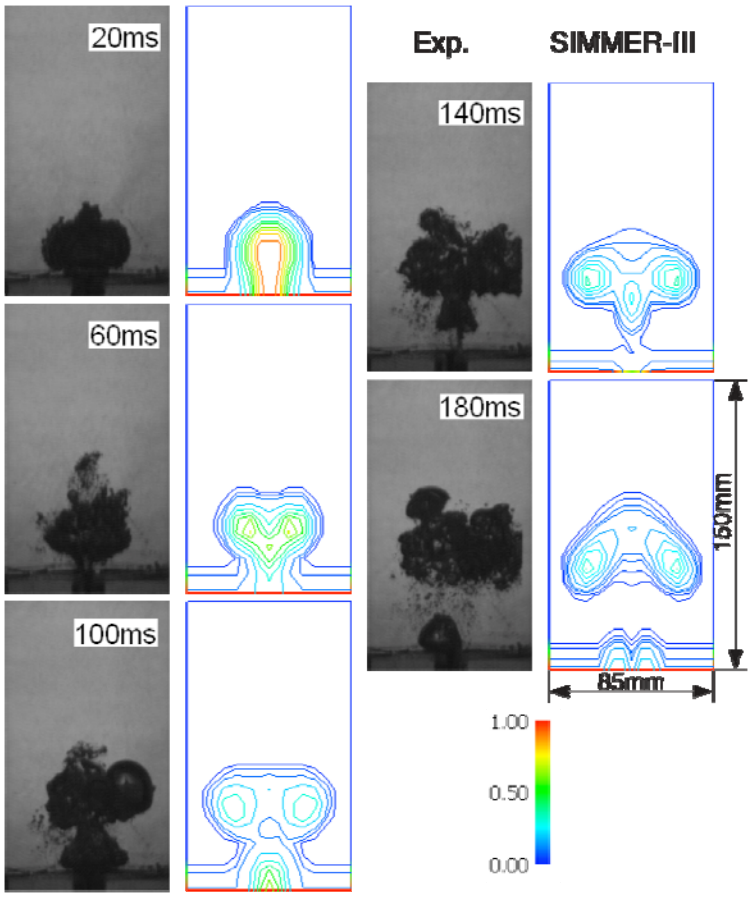

Fig. 35: Comparison between experimental and simulated bubble images of the reference case 3.

The color bar shows the vapor volume fraction of the contour lines in the SIMMER-III simulation results.

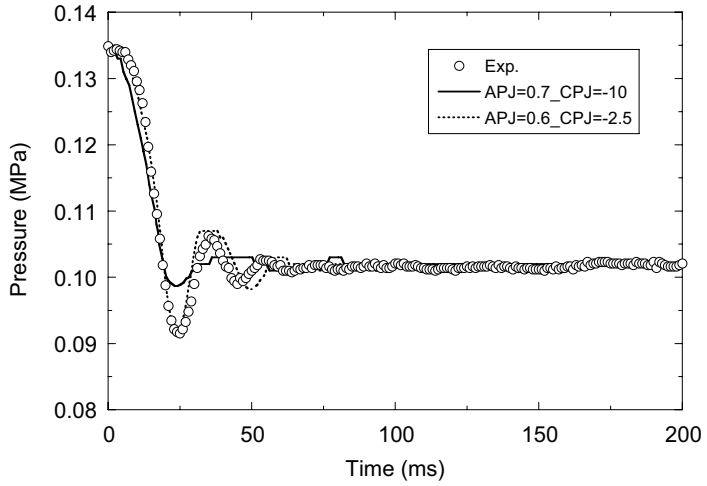

Fig. 36: Pressure transient in the pressure vessel of the case I.

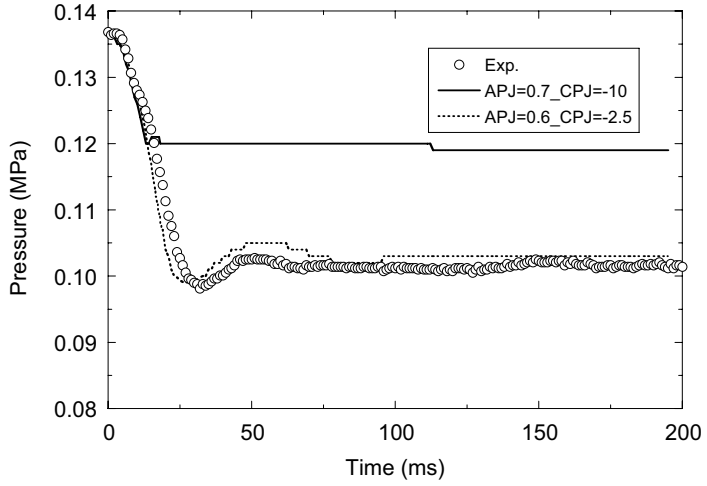

Fig. 37: Pressure transient in the pressure vessel of the case II.

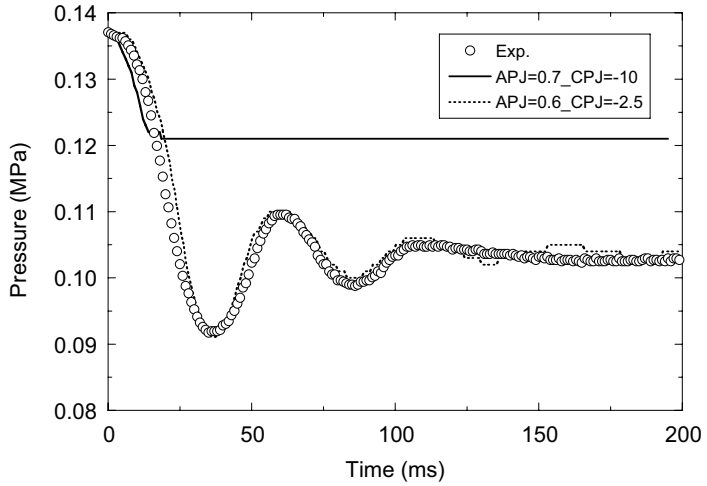

Fig. 38: Pressure transient in the pressure vessel of the case III.

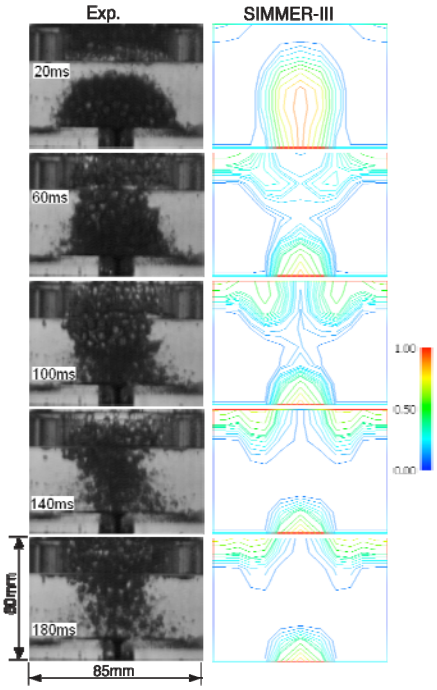

Fig. 39: Comparison between experimental and simulated bubble images of the case I.

The color bar shows the vapor volume fraction of the contour lines in the SIMMER-III simulation results. The simulation results are obtained with $\alpha_{PJ\max} = 0.6$ and $C_{PJ} = -2.5$.

Fig. 40: Comparison between experimental and simulated particle bed images of the case I.

The color bars show the volume fraction of solid particles in the SIMMER-III simulation results. The simulation results are obtained with $\alpha_{PJ\max} = 0.6$ and $C_{PJ} = -2.5$.

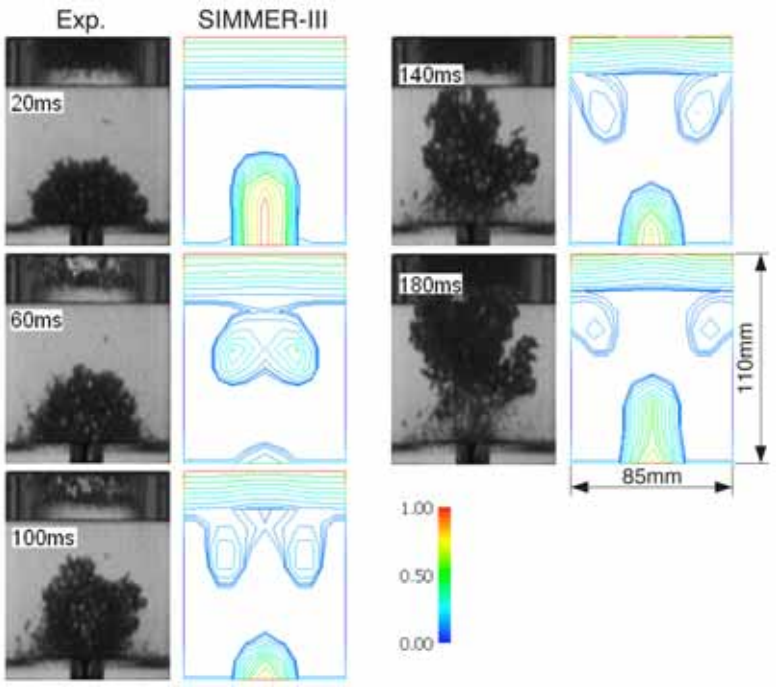

Fig. 41: Comparison between experimental and simulated bubble images of the case II.

The color bar shows the vapor volume fraction of the contour lines in the SIMMER-III simulation results. The simulation results are obtained with $\alpha_{PJ\max} = 0.6$ and $C_{PJ} = -2.5$.

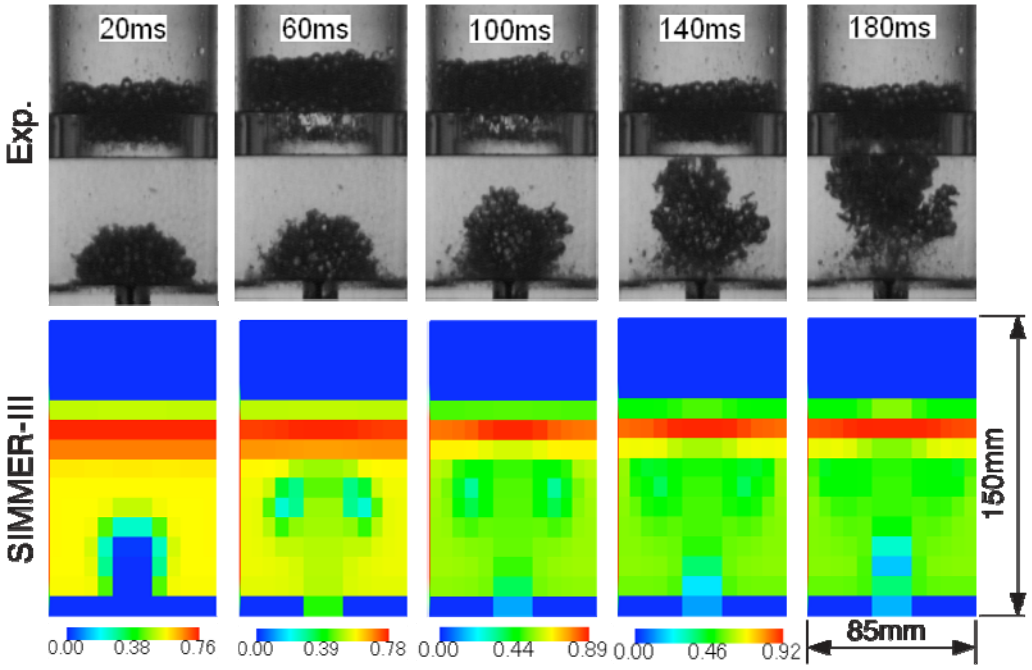

Fig. 42: Comparison between experimental and simulated particle bed images of the case II.

The color bars show the volume fraction of solid particles in the SIMMER-III simulation results. The simulation results are obtained with $\alpha_{PJ\max} = 0.6$ and $C_{PJ} = -2.5$.

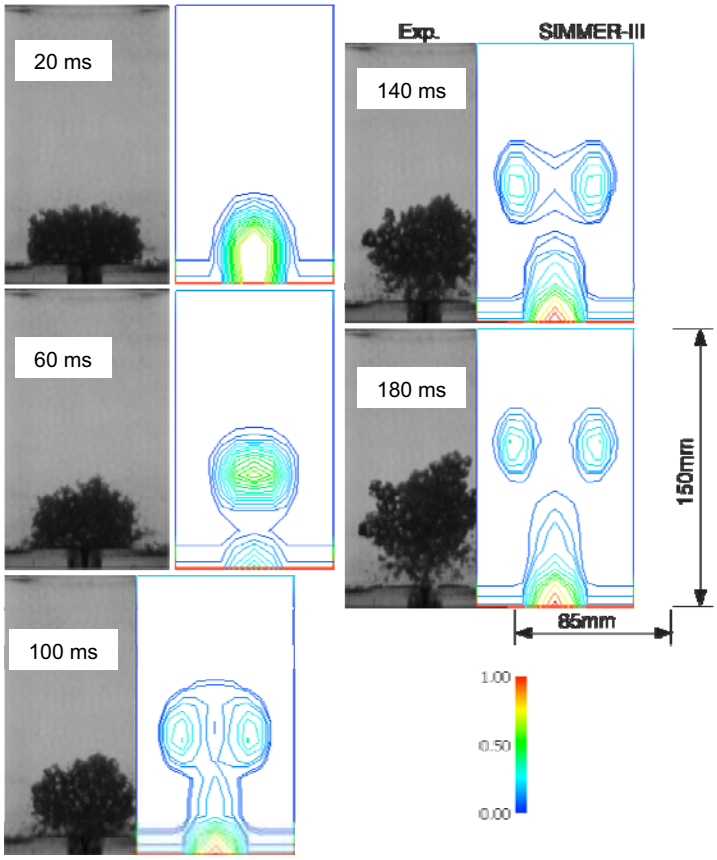

Fig. 43: Comparison between experimental and simulated bubble images of the case III.

The color bar shows the vapor volume fraction of the contour lines in the SIMMER-III simulation results. The simulation results are obtained with $\alpha_{PJ\max} = 0.6$ and $C_{PJ} = -2.5$.

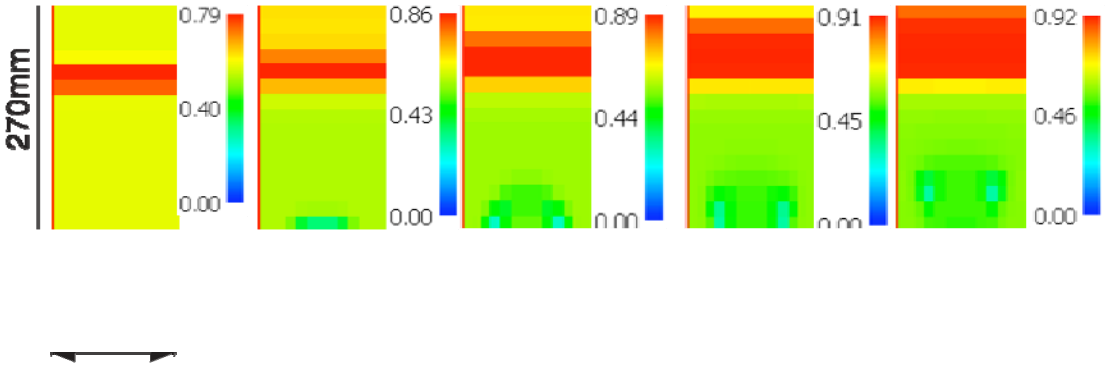

Fig. 44: Simulated particle bed images of the case III.

The color bars shows the volume fraction of solid particles in the SIMMER-III simulation results. The simulation results are obtained with $\alpha_{PJ\max} = 0.6$ and $C_{PJ} = -2.5$.

国際単位系（SI）

表１．SI 基本単位

基本量	SI 基本単位	
	名称	記号
長さ	メートル	m
質量	キログラム	kg
時間	秒	s
電流	アンペア	A
熱力学温度	ケルビン	K
物質量	モル	mol
光度	カンデラ	cd

表２．基本単位を用いて表されるSI組立単位の例

組立量	SI 基本単位	
	名称	記号
面積	平方メートル	m^2
体積	立法メートル	m^3
速さ，速度	メートル毎秒	m/s
加速度	メートル毎秒毎秒	m/s^2
波数	毎メートル	m^{-1}
密度，質量密度	キログラム毎立方メートル	kg/m^3
面積密度	キログラム毎平方メートル	kg/m^2
比体積	立方メートル毎キログラム	m^3/kg
電流密度	アンペア毎平方メートル	A/m^2
磁界の強さ	アンペア毎メートル	A/m
量濃度[a]，濃度	モル毎立方メートル	mol/m^3
質量濃度	キログラム毎立法メートル	kg/m^3
輝度	カンデラ毎平方メートル	cd/m^2
屈折率[b]	（数字の） 1	1
比透磁率[b]	（数字の） 1	1

(a) 量濃度（amount concentration）は臨床化学の分野では物質濃度（substance concentration）ともよばれる。
(b) これらは無次元量あるいは次元１をもつ量であるが、そのことを表す単位記号である数字の１は通常は表記しない。

表３．固有の名称と記号で表されるSI組立単位

組立量	SI 組立単位			
	名称	記号	他のSI単位による表し方	SI基本単位による表し方
平面角	ラジアン[b]	rad	1[b]	m/m
立体角	ステラジアン[b]	sr[c]	1[b]	m^2/m^2
周波数	ヘルツ[d]	Hz		s^{-1}
力	ニュートン	N		m kg s^{-2}
圧力，応力	パスカル	Pa	N/m^2	m^{-1} kg s^{-2}
エネルギー，仕事，熱量	ジュール	J	N m	m^2 kg s^{-2}
仕事率，工率，放射束	ワット	W	J/s	m^2 kg s^{-3}
電荷，電気量	クーロン	C		s A
電位差（電圧），起電力	ボルト	V	W/A	m^2 kg s^{-3} A^{-1}
静電容量	ファラド	F	C/V	m^{-2} kg^{-1} s^4 A^2
電気抵抗	オーム	Ω	V/A	m^2 kg s^{-3} A^{-2}
コンダクタンス	ジーメンス	S	A/V	m^{-2} kg^{-1} s^3 A^2
磁束	ウエーバ	Wb	Vs	m^2 kg s^{-2} A^{-1}
磁束密度	テスラ	T	Wb/m^2	kg s^{-2} A^{-1}
インダクタンス	ヘンリー	H	Wb/A	m^2 kg s^{-2} A^{-2}
セルシウス温度	セルシウス度[e]	℃		K
光束	ルーメン	lm	cd sr[c]	cd
照度	ルクス	lx	lm/m^2	m^{-2} cd
放射性核種の放射能[f]	ベクレル[d]	Bq		s^{-1}
吸収線量，比エネルギー分与，カーマ	グレイ	Gy	J/kg	m^2 s^{-2}
線量当量，周辺線量当量，方向性線量当量，個人線量当量	シーベルト[g]	Sv	J/kg	m^2 s^{-2}
酸素活性	カタール	kat		s^{-1} mol

(a)SI接頭語は固有の名称と記号を持つ組立単位と組み合わせても使用できる。しかし接頭語を付した単位はもはやコヒーレントではない。
(b)ラジアンとステラジアンは数字の１に対する単位の特別な名称で、量についての情報をつたえるために使われる。実際には、使用する時には記号rad及びsrが用いられるが、習慣として組立単位としての記号である数字の１は明示されない。
(c)測光学ではステラジアンという名称と記号srを単位の表し方の中に、そのまま維持している。
(d)ヘルツは周期現象についてのみ、ベクレルは放射性核種の統計的過程についてのみ使用される。
(e)セルシウス度はケルビンの特別な名称で、セルシウス温度を表すために使用される。セルシウス度とケルビンの単位の大きさは同一である。したがって、温度差や温度間隔を表す数値はどちらの単位で表しても同じである。
(f)放射性核種の放射能（activity referred to a radionuclide）は、しばしば誤った用語で"radioactivity"と記される。
(g)単位シーベルト（PV,2002,70,205）についてはCIPM勧告2（CI-2002）を参照。

表４．単位の中に固有の名称と記号を含むSI組立単位の例

組立量	SI 組立単位		
	名称	記号	SI 基本単位による表し方
粘度	パスカル秒	Pa s	m^{-1} kg s^{-1}
力のモーメント	ニュートンメートル	N m	m^2 kg s^{-2}
表面張力	ニュートン毎メートル	N/m	kg s^{-2}
角速度	ラジアン毎秒	rad/s	m m^{-1} s^{-1}=s^{-1}
角加速度	ラジアン毎秒毎秒	rad/s^2	m m^{-1} s^{-2}=s^{-2}
熱流密度，放射照度	ワット毎平方メートル	W/m^2	kg s^{-3}
熱容量，エントロピー	ジュール毎ケルビン	J/K	m^2 kg s^{-2} K^{-1}
比熱容量，比エントロピー	ジュール毎キログラム毎ケルビン	J/(kg K)	m^2 s^{-2} K^{-1}
比エネルギー	ジュール毎キログラム	J/kg	m^2 s^{-2}
熱伝導率	ワット毎メートル毎ケルビン	W/(m K)	m kg s^{-3} K^{-1}
体積エネルギー	ジュール毎立方メートル	J/m^3	m^{-1} kg s^{-2}
電界の強さ	ボルト毎メートル	V/m	m kg s^{-3} A^{-1}
電荷密度	クーロン毎立方メートル	C/m^3	m^{-3} sA
表面電荷	クーロン毎平方メートル	C/m^2	m^{-2} sA
電束密度，電気変位	クーロン毎平方メートル	C/m^2	m^{-2} sA
誘電率	ファラド毎メートル	F/m	m^{-3} kg^{-1} s^4 A^2
透磁率	ヘンリー毎メートル	H/m	m kg s^{-2} A^{-2}
モルエネルギー	ジュール毎モル	J/mol	m^2 kg s^{-2} mol^{-1}
モルエントロピー，モル熱容量	ジュール毎モル毎ケルビン	J/(mol K)	m^2 kg s^{-2} K^{-1} mol^{-1}
照射線量（X線及びγ線）	クーロン毎キログラム	C/kg	kg^{-1} sA
吸収線量率	グレイ毎秒	Gy/s	m^2 s^{-3}
放射強度	ワット毎ステラジアン	W/sr	m^4 m^{-2} kg s^{-3}=m^2 kg s^{-3}
放射輝度	ワット毎平方メートル毎ステラジアン	$W/(m^2 sr)$	m^2 m^{-2} kg s^{-3}=kg s^{-3}
酵素活性濃度	カタール毎立方メートル	kat/m^3	m^{-3} s^{-1} mol

表５．SI 接頭語

乗数	接頭語	記号	乗数	接頭語	記号
10^{24}	ヨタ	Y	10^{-1}	デシ	d
10^{21}	ゼタ	Z	10^{-2}	センチ	c
10^{18}	エクサ	E	10^{-3}	ミリ	m
10^{15}	ペタ	P	10^{-6}	マイクロ	μ
10^{12}	テラ	T	10^{-9}	ナノ	n
10^9	ギガ	G	10^{-12}	ピコ	p
10^6	メガ	M	10^{-15}	フェムト	f
10^3	キロ	k	10^{-18}	アト	a
10^2	ヘクト	h	10^{-21}	ゼプト	z
10^1	デカ	da	10^{-24}	ヨクト	y

表６．SIに属さないが、SIと併用される単位

名称	記号	SI 単位による値
分	min	1 min=60s
時	h	1h =60 min=3600 s
日	d	1 d=24 h=86 400 s
度	°	1°=(π/180) rad
分	’	1’=(1/60)°=(π/10800) rad
秒	”	1”=(1/60)’=(π/648000) rad
ヘクタール	ha	$1ha=1hm^2=10^4m^2$
リットル	L, l	$1L=11=1dm^3=10^3cm^3=10^{-3}m^3$
トン	t	$1t=10^3$ kg

表７．SIに属さないが、SIと併用される単位で、SI単位で表される数値が実験的に得られるもの

名称	記号	SI 単位で表される数値
電子ボルト	eV	$1eV=1.602\ 176\ 53(14)\times10^{-19}J$
ダルトン	Da	$1Da=1.660\ 538\ 86(28)\times10^{-27}kg$
統一原子質量単位	u	1u=1 Da
天文単位	ua	$1ua=1.495\ 978\ 706\ 91(6)\times10^{11}m$

表８．SIに属さないが、SIと併用されるその他の単位

名称	記号	SI 単位で表される数値
バール	bar	1 bar=0.1MPa=100kPa=10^5Pa
水銀柱ミリメートル	mmHg	1mmHg=133.322Pa
オングストローム	Å	1 Å=0.1nm=100pm=10^{-10}m
海里	M	1 M=1852m
バーン	b	$1 b=100fm^2=(10^{-12}cm)2=10^{-28}m^2$
ノット	kn	1 kn=(1852/3600)m/s
ネーパ	Np	SI単位との数値的な関係は、対数量の定義に依存。
ベル	B	
デジベル	dB	

表９．固有の名称をもつCGS組立単位

名称	記号	SI 単位で表される数値
エルグ	erg	$1 erg=10^{-7}$ J
ダイン	dyn	$1 dyn=10^{-5}$N
ポアズ	P	1 P=1 dyn s cm^{-2}=0.1Pa s
ストークス	St	1 St =$1cm^2$ s^{-1}=$10^{-4}m^2$ s^{-1}
スチルブ	sb	1 sb =1cd cm^{-2}=10^4cd m^{-2}
フォト	ph	1 ph=1cd sr cm^{-2} 10^4lx
ガル	Gal	1 Gal =1cm s^{-2}=$10^{-2}ms^{-2}$
マクスウェル	Mx	1 Mx = 1G cm^2=10^{-8}Wb
ガウス	G	1 G =1Mx cm^{-2} =10^{-4}T
エルステッド[c]	Oe	1 Oe ≙ $(10^3/4π)$A m^{-1}

(c) 3元系のCGS単位系とSIでは直接比較できないため、等号「 ≙ 」は対応関係を示すものである。

表10．SIに属さないその他の単位の例

名称	記号	SI 単位で表される数値
キュリー	Ci	$1 Ci=3.7\times10^{10}Bq$
レントゲン	R	$1 R=2.58\times10^{-4}C/kg$
ラド	rad	$1 rad=1cGy=10^{-2}Gy$
レム	rem	$1 rem=1 cSv=10^{-2}Sv$
ガンマ	γ	1γ=1 nT=10-9T
フェルミ		1フェルミ=1 fm=10-15m
メートル系カラット		1メートル系カラット = 200 mg = 2×10-4kg
トル	Torr	1 Torr = (101 325/760) Pa
標準大気圧	atm	1 atm = 101 325 Pa
カロリー	cal	1cal=4.1858J（「15℃」カロリー），4.1868J（「IT」カロリー）4.184J（「熱化学」カロリー）
ミクロン	μ	1 μ =1μm=10^{-6}m

（第8版，2006年改訂）